

Article

Micro-Scale Lattice Boltzmann Simulation of Two-Phase CO₂–Brine Flow in a Tighter REV Extracted from a Permeable Sandstone Core: Implications for CO₂ Storage Efficiency

Yidi Wan ¹, Chengzao Jia ^{2,*}, Wen Zhao ³, Lin Jiang ³ and Zhuxin Chen ³¹ School of Earth and Space Sciences, Peking University, Beijing 100871, China² PetroChina Company Ltd., Beijing 100011, China³ Research Institute of Petroleum Exploration and Development, Beijing 100083, China* Correspondence: jiacz@petrochina.com.cn

Abstract: Deep saline permeable sandstones have the potential to serve as sites for CO₂ storage. However, unstable CO₂ storage in pores can be costly and harmful to the environment. In this study, we used lattice Boltzmann (LB) simulations to investigate the factors that affect steady-state CO₂–brine imbibition flow in sandstone pores, with a focus on improving CO₂ storage efficiency in deep saline permeable sandstone aquifers. We extracted three representative element volumes (REVs) from a digital rock image of a sandstone core and selected a tighter REV in the upper subdomain so that its permeability would apparently be lower than that of the other two based on single-phase LB simulation for further analysis. The results of our steady-state LB simulations of CO₂–brine imbibition processes in the tighter REV under four differential pressures showed that a threshold pressure gradient of around 0.5 MPa/m exists at a differential pressure of 200 Pa, and that higher differential pressures result in a greater and more linear pressure drop and stronger channelization after the flow are initiated. Furthermore, we conducted simulations over a range of target brine saturations in the tighter REV at the optimal differential pressure of 400 Pa. Our findings showed that the relative permeability of CO₂ is greatly reduced as the capillary number falls below a certain threshold, while the viscosity ratio has a smaller but still significant effect on relative permeability and storage efficiency through the lubrication effect. Wettability has a limited effect on the storage efficiency, but it does impact the relative permeability within the initial saturation range when the capillary number is low and the curves have not yet converged. Overall, these results provide micro-scale insights into the factors that affect CO₂ storage efficiency in sandstones.

Keywords: CO₂ storage efficiency; CO₂–brine flow; lattice Boltzmann; sandstone; digital rock image; REV; steady state



Citation: Wan, Y.; Jia, C.; Zhao, W.; Jiang, L.; Chen, Z. Micro-Scale Lattice Boltzmann Simulation of Two-Phase CO₂–Brine Flow in a Tighter REV Extracted from a Permeable Sandstone Core: Implications for CO₂ Storage Efficiency. *Energies* **2023**, *16*, 1547. <https://doi.org/10.3390/en16031547>

Academic Editors: Bin Pan, Shaojie Zhang and Gang Hui

Received: 13 December 2022

Revised: 14 January 2023

Accepted: 23 January 2023

Published: 3 February 2023



Copyright: © 2023 by the authors. Licensee MDPI, Basel, Switzerland. This article is an open access article distributed under the terms and conditions of the Creative Commons Attribution (CC BY) license (<https://creativecommons.org/licenses/by/4.0/>).

1. Introduction

Climate change and induced greenhouse effects mainly caused by excessive CO₂ emissions by human activities pose great challenges to the earth system [1–5]. CO₂ emitted in the atmosphere is mainly sourced from the combustion of fossil fuels and electricity generated from the power plants. Amid a great variety of solutions to this problem, CO₂ capture and sequestration (CCS) are assumed to be efficient techniques [6,7]. CCS entails the separation of CO₂ from other substances produced by power plants or other similar human industrial activities, the compression and transportation of them to the storage sites and the injection of supercritical CO₂ into onshore or offshore geological formations that provide ample storage space [8,9]. In this sense, the geological capture and sequestration of CO₂ is crucial for mitigating the negative impact of climate change and derived environmental issues [6,10,11]. In addition, most of geological formations that are idealized candidates for CO₂ storage are deep saline sandstone reservoirs, which are permeable and widely distributed worldwide [12–14]. According to [15], the confidence level of CO₂ storage

efficiency in sandstone aquifers (90% or higher) is much higher than that for limestone ones (5%). Meanwhile, the preferable mineralogy and geochemistry of sandstone saline aquifers provide exceptional strengths for the selection [16–18]. Several experimental investigations [18–22] at the macroscopic scale in the literature have been conducted on sandstones, with results showing the big variance in storage efficiency, depending on sandstone type but also complicated pore structure inside. As a result, the stable storage efficiency of CO₂ from sandstones is still a research hotspot and is yet to be fully evaluated at a microscopic scale. Since one can rarely bear the great cost of the unstable CO₂ storage after the CCS operation, which could give rise to large economic losses and secondary environmental consequences [23–26], a better and integrated understanding of the physics of two-phase CO₂–brine flow in the porosity of sandstones is extraordinarily essential for preventing CO₂ leakage from the formation pores by serving as permanent storage. As such, one must develop reliable models in addition to experimental measurements for both the sandstone formation and the physics of two-phase CO₂–brine flow in it.

Multiscale structure of the sandstone formations and the fact that various length scales exist, ranging from pore [9,27–29] to core [30–32], macroscopic up until reservoir scale [9,29,33]. They necessitate the development of different models at each scale and the integration of all of them into a uniform framework that characterizes the heterogeneities and anisotropy involved [10]. Meanwhile, the injection of supercritical CO₂ into a deep saline brine aquifer leads to complicated two-phase flow mechanisms in rock pore systems that are mainly dependent on pore space, pore size distribution and nondimensional parameters such as wettability, viscosity ratio and capillary number, etc. [28,33–35]. Even though the numerous traditional experimental methods [30–32,36] at core scale were used to study the constitutive relations such as capillary pressure and relative permeability curves, which can then be applied into large-scale continuum-based CFD simulators [37–39], the implementation of these experiments is highly complicated, expensive, and time-costly, with great measurement uncertainties that are unquantifiable. Moreover, due to the heterogeneity of a sizeable number of rock samples we encounter in the reality, simply treating the rock sample as a continuum material with uniform macroscopic petrophysical properties is a less effective method for uncovering various micro-scale mechanisms of fluid flow in the pore structures. Given the challenges for experimental studies and continuum-based simulation methods, the pore-scale numerical simulation of fluid flow in porous media is increasingly preferable for understanding phase behaviors and fluid–solid and fluid–fluid interactions in both quantitative and visually intuitive ways. Over the last few years, pore-scale numerical investigations have gained great popularity, especially with respect to their applications in brine aquifers. New techniques, such as X-ray CT scan and imaging, have gradually been applied to pore-scale and REV (representative elementary volume)-scale visualizations of multiphase flow in porous media [40–44].

The numerical methods of simulating flow behaviors in porous media and calculating relevant flow properties can be categorized into direct modeling and pore network modeling methods [44]. For the latter methods, a network representing the rock pore system is extracted and reconstructed based on principles of topology [45,46], and this is then utilized to simulate the flow pattern of single-phase and multiphase flow in it by solving the fluid dynamical governing equations. Although this approach features many remarkable strengths, such as fast computational speeds and finer resolution that satisfy any specific demands for engineering projects, the geometric oversimplification of its pore network with nodes and bonds can cause large, challenging errors in the simulation results [47,48]. The direct modeling approach, by contrast, solves the transport governing equations based on real digital images (micro-CT [40], SEM [49], i.e.,) of rocks, ensuring the physical fidelity of computational results and more importantly that the rock sample itself is not damaged. As a result, one can directly simulate two-phase flow in these images, which renders them better models better than those unnecessarily developed by numerical methods such as the Gaussian field method [50], simulated annealing algorithm [51], Markov chain Monte Carlo [52], etc. For such pore-scale research, several CFD methods have been extensively

applied through numerically solving the Navier–Stokes or NS equation that guarantees the momentum conservation, such as the lattice Boltzmann method (LBM) [27], finite element method (FEM) [53], finite volume method (FVM) [54] and finite difference method (FDM) [55]. The NS equation is a partial differential equation of the second order that requires intricate discretization and, therefore, results in demanding programming [56]. In addition, the nonlinear convective term in the NS equation presents numerous numerical challenges [57,58]. Therefore, solving the NS equation in complex porous media, like characterized by highly heterogeneous rocks, either requires simplifying the medium's geometrical characteristics or using complex grids that necessitate extensive computations. In comparison with other methods, LBM solves the discrete Boltzmann equation with a specific collision model rather than the conventional NS equation. Moreover, it can be effectively applied into pore-scale modelings by associating itself with physics involved in a series of interactions in the pore space. At the same time, it also easily handles complex pore geometries by voxelizing them into discrete nodes that match the lattices in its numerical scheme [58]. With the rapid evolution of computational power and platforms represented by graphical processing unit (GPU)-enhanced parallel computations [59], the large-scale LB-based simulation of multiphase flow in 3D complicated pore space has been realized and also empowered with finer resolution, higher accuracy of results and faster running speed.

To the best of our knowledge, two-phase CO₂–brine flow has been extensively reported using the lattice Boltzmann method with its great advantages of modeling irregular flow pathways in complex pore geometries and coupling both fluid–fluid and fluid–solid interactions. Common two-phase LB models are composed of the color–gradient model [60], the pseudopotential model [61], the free energy model [62] and the phase-field model [27]. Though all of these types of LB models have been extensively utilized to simulate multiphase immiscible flow in porous media at pore scale, the color–gradient model and the free energy model show up better performance in handling high viscosity ratios and maintaining a sharp interface between two immiscible fluids [63]. Nevertheless, the color–gradient is more preferred for simulating immiscible multiphase flow in heterogeneous porous media under scenarios of low capillary numbers with good accuracy and efficiency [9]. Most of the literature [28,33,34,48] adopting the color LB model for modeling two-phase CO₂–brine flow in rocks is based on pore-scale models, which needs detailed geometrical information and is characterized by a computation domain that is very small and thus inapplicable to field-scale practices [64]. An alternative method to it is the representative elementary volume (REV)-scale method, which is much larger than the pore scale and smaller than the field scale [45]. One of the greatest advantages of the REV-scale method is that some inessential pore structures at the micro scale can be overlooked and statistical flow properties such as permeability, velocity and pressure can be obtained through semi-empirical relations such as the Darcy's law [65] and Brinkman-extended Darcy models [66], etc.

2. Motivation and Organization for This Study

As far as we are concerned, most of the previous studies regarding micro-scale LB simulation of two-phase CO₂–brine flow in sandstone rocks mainly focused on pore-scale insights into the mechanism and flow properties such as relative permeability of the flow processes [19,21,25,26]. Few of them, however, made efforts into quantitatively considering CO₂ storage efficiency due to the two-phase immiscible flow at REV scale, especially the imbibition processes in the complex pore space. Meanwhile, some of other studies [50–52] in the literature, which apply the generally simplified 2D or 3D pore models generated by computer modeling, can hardly consider the complexity and heterogeneity of sandstone rocks themselves as porous media. Accordingly, we are motivated in this study to understand the CO₂ storage efficiency quantitatively due to the two-phase imbibition processes in the heterogeneous sandstones, as illustrated in Figure 1, at REV scale.

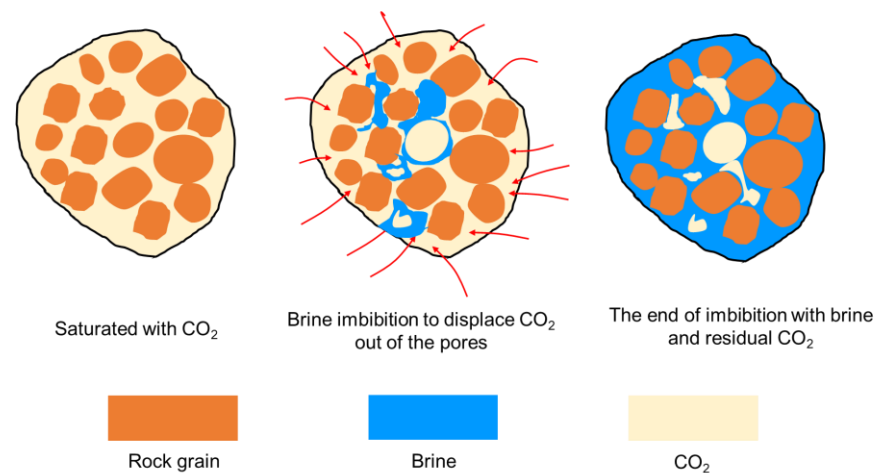


Figure 1. Schematic showing the CO₂ unstable storage due to two-phase CO₂–brine imbibition processes where the pore space saturated with CO₂ (left) is flooded by brine, resulting in the displacement of in situ CO₂ out of the pores (middle), until finally only the residual CO₂ and brine are left in the pore space (right).

In this work, we aim at a micro-scale understanding of CO₂ storage efficiency in a tighter REV extracted from a permeable heterogeneous sandstone rock sample based on LB simulation of steady-state CO₂–brine imbibition processes, since the tighter subdomain is assumed to have the relative higher storage efficiency with higher capillary threshold for brine breakthrough. Firstly, REV analysis was utilized to extract 3 REV representing the upper, middle, and lower space of the whole core in which pore space was reconstructed using a series of image processing sections, including image preprocessing, filtering, and threshold segmentation. In addition, single-phase LB simulations were conducted on each of these 3 REVs and their calculated results including petrophysical properties and physical fields (pressure; velocity) were further analyzed in order to identify a tighter REV that its central part was then cut as prepared as boundary conditions for subsequent two-phase LB simulations of CO₂–brine imbibition flow in it. Two main parts were involved: 1. Modellings were conducted on the tighter subsample under 4 differential pressures (100 Pa; 200 Pa; 300 Pa; 400 Pa) to identify if threshold a pressure gradient [67–71] below which no flow in the computational domain is driven exists and find out the optimized value under which the pore space is fully channelized as characteristics of Darcy flow. 2. We conducted LB simulation of the steady-state CO₂–brine imbibition processes over a span of target saturations on the tighter REV under 18 scenarios with different combinations of nondimensional parameters including wettability index, capillary number and viscosity ratio under the optimized differential pressure previously obtained to reveal relative permeability curves of CO₂ under different combinations of three nondimensional parameters. On this basis, we further evaluated CO₂ storage efficiency in these different cases by estimating its residual saturation through setting a lower bound of $kr_{CO_2} = 0.05$.

The organization of the remaining part of this paper is as follows: the next section is mainly concerned with the methodologies involved in this study. In Section 3.2, methodology for digital rock reconstruction and pore space extraction through image scanning and processing techniques are introduced and single-phase LB model, multiphase color-gradient LB model and the derived steady-state LBPM (lattice Boltzmann porous method) are, respectively interpreted in Section 3.2, Section 3.3, and Section 3.4. Results of and discussions on single-phase, two-phase LB simulations and CO₂ storage efficiency, based on relative permeability under conditions of various combinations of nondimensional parameters, are analyzed and presented in Section 4, while the main results of the paper are summarized in Section 5 as conclusions. Besides, Section 6 or the last section has been especially created for this paper to demonstrate the expectations and limitations of this study for future work.

3. Methodology

3.1. Digital Rock Reconstruction and REV Analysis

The sample rock in this study is a sandstone extracted from the Daqing Oilfield at a depth of approximately 2047 m. Its porosity and permeability have been measured to be 14.46% and 450 mD, respectively. The main mineralogy of the rock was found to be quartz (75.714%), feldspar (14.65%), and other minerals including clay, calcite, dolomite, and pyrite were also present (less than 10% combined). A X-ray micro-CT imaging device, manufactured by Zeiss GMBH, based in Oberkochen, Germany, at RIPED (Research Institute of Petroleum Exploration and Development), Beijing, was used to scan the rock sample, generating a series of gray-scale scans like Figure 2, in which nearly no fracture was present and pore space is well preserved. These resemble the petrophysical properties of Berea sandstone [28,72]. Some brighter or darker patches are seen in these CT scans, like Figure 2, because various minerals in our rock sample have different densities and then feature different attenuation coefficients for X rays. However, the mineralogical distribution within our sample would not impact our simulation in the following part. A stack of 1400 CT scans like Figure 2 with size of 1998×2006 pixels and resolution of $1.98 \mu\text{m}$ is reconstructed as a 3D digital rock with dimension of $1998 \times 2006 \times 1400$ voxels. To the best of our best knowledge, running efficient LB simulations of fluid flow in porous media like rocks requires graphics processing unit (GPU)-based parallel computing technologies, instead of a computing processing unit (CPU). Therefore, conducting LB simulations of the digital rock image of the whole-core rock sample is hardly realized on personal computers (PC) and, even with HPCC, it would inevitably result in big time consumption [36,64]. As a result, a careful study is needed to identify the size of a representative elementary volume (REV) for different areas in a whole digital rock that is prepared for flow simulation. In order to demonstrate the properties of different regions of the 3D digital rock images, REV analysis in terms of porosity, which is calculated through a series of image processing sections including filtering, threshold-segmentation (Figure 3), combined with central cutting method [73,74], as illustrated in Figure 4, is conducted on the three subdomains (upper, middle, and bottom) of the whole-core computational domain as shown in Figure 5. Figure 6 demonstrates that spatial porosity correlations with REV lengths for REV1 and REV2 converge at 300 voxels, and the convergence is at 350 voxels for REV3. These conclusions are based on the approximation criterion that the porosity difference varies by less than 2% with the REV length since the convergence length. To follow up on the following flow simulations where a tighter REV was needed, we decided to establish 3 REVs with size of $800 \times 800 \times 400$ voxels (Figure 7) in order to sufficiently overlap a tighter REV in the whole-core domain of the rock sample. The calculated porosities for REV1, REV2 and REV3 are 10.654%, 8.642% and 16.721%.

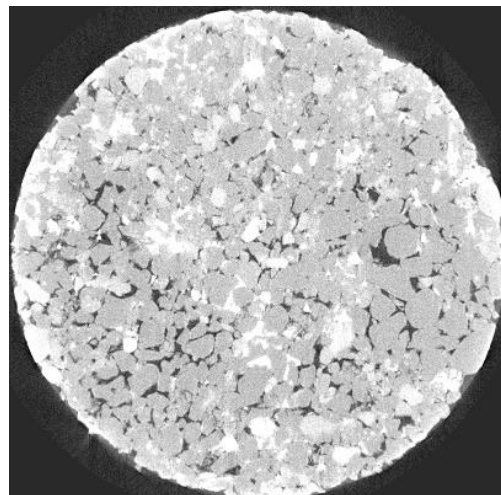


Figure 2. Example of gray-scale micro-CT scan of sandstone rock sample in this study.

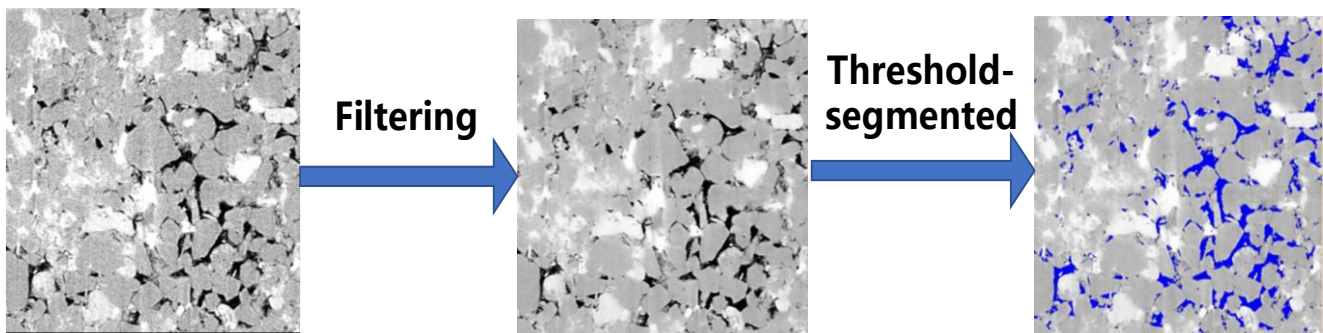


Figure 3. Workflow for imaging processing of raw CT image (left, e.g.,) through filtering, obtaining the noise-free image which is further threshold-segmented into separated pore space (blue) and rock matrix (gray) on the right.

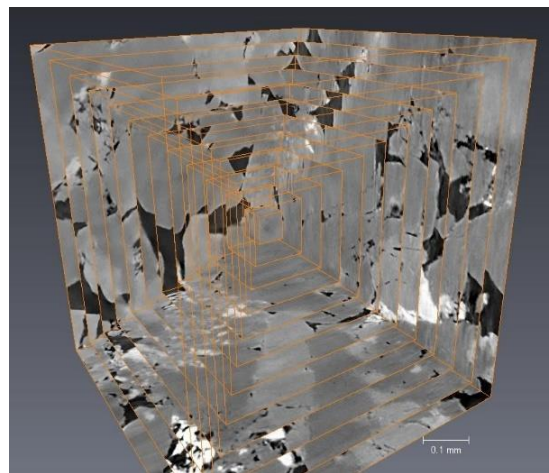


Figure 4. Schematic diagram showing REV central cutting.

Whole-core domain of rock sample

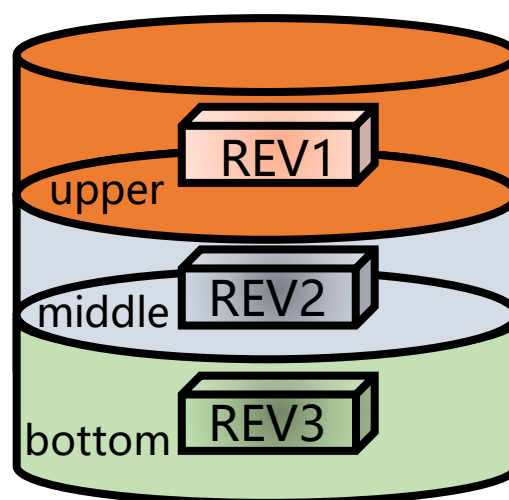


Figure 5. Schematic diagram of REV orientations at three different subdomains (upper (orange), middle (gray) and bottom (green)) divided from a whole-core computational domain of CT-scanned rock sample.

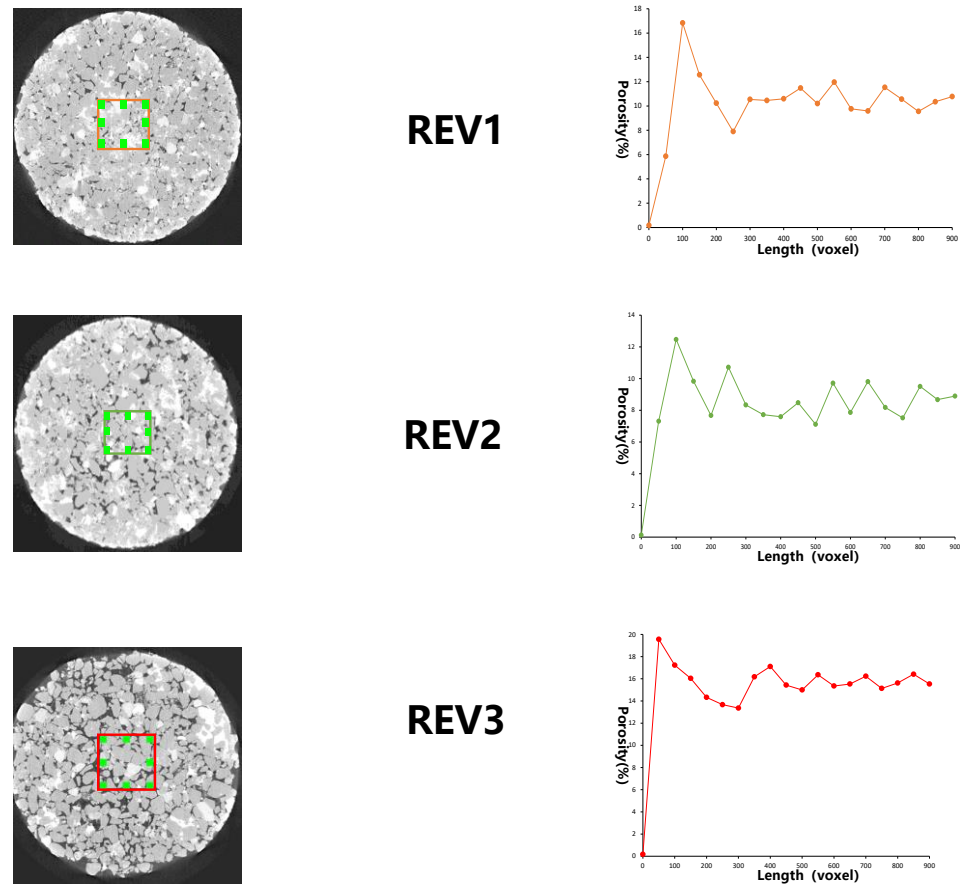


Figure 6. Results of REV analysis in terms of porosity spatial correlation (right), performed on three parts of the whole core domain defined in Figure 5, based on the REV central cutting method explained in Figure 5 with top view presented on the left.

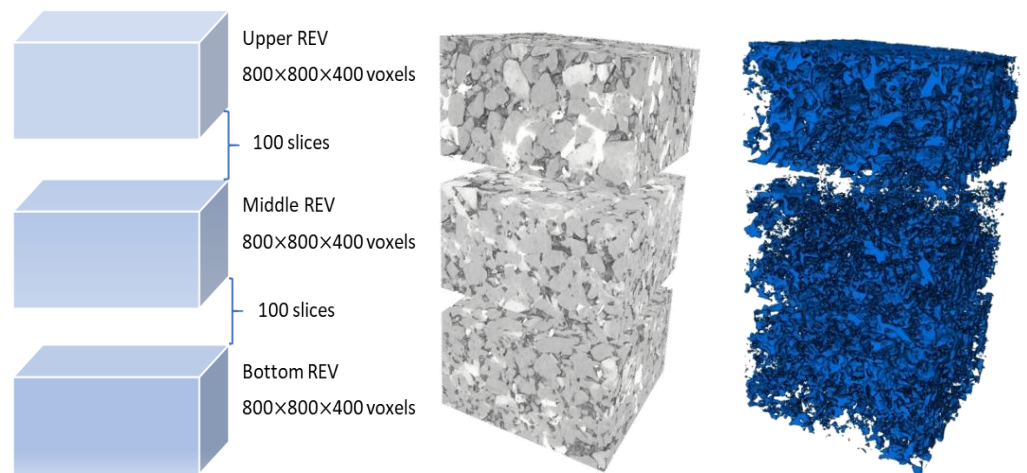


Figure 7. Schematic plot showing spatial position (left), gray-scale CT image (middle) and extracted pore space (right) of REV characterizing upper, middle, and bottom subdomains of the whole-core domain.

3.2. Single-Phase LB Model

As we all know, the main role that lattice Boltzmann method plays is linking micro-scale mechanisms and macro-scale flow properties possessed as a mesoscopic media such as pressure and velocity [75]. Specifically, the whole computational domain is discretized into many of lattices containing conceptualized groups of fluid particles. In fact, their physical

transport is governed by mass and momentum conservative equations [76–78]. In addition, the fluid-solid, fluid-fluid interactions can be well characterized using the LB method by utilizing the forces balance between groups of molecules, rather than tracking individual molecules [79] and the Navier–Stokes equation can then be recovered by application of a Taylor series expansion of the lattice Boltzmann equation, followed by the Chapman–Enskog expansion [80]. The particle distribution function $f_i(x, t)$ at position x and time t in the i th velocity direction is assigned at each lattice node. In this chapter, the single-phase LB model is established as follows:

According to the LB equation with the Bhatnagar–Gross–Krook (BGK) approximation, the evolution of $f_i(x, t)$ can be defined as follows:

$$f_i(x + e_i \Delta t, t + \Delta t) - f_i(x, t) = -\frac{1}{\tau} [f_i(x, t) - f_i^{eq}(x, t)] \tag{1}$$

where $f_i(x, t)$ and $f_i^{eq}(x, t)$ represent the non-equilibrium and equilibrium distribution functions, respectively; Δt is a timestep, τ is the relaxation time as a good measure of how quickly the flow system evolves from non-equilibrium to equilibrium state, related to kinematic viscosity (ν) and written as $\tau = \nu / (c_s^2 s \times \Delta t) + 0.5$ with sound speed $c_s = 1/\sqrt{3}$.

In general, the lattice Boltzmann equation is divided into two steps: streaming (Equation (2)) and collision (Equation (3)):

$$f_i(x + e_i \Delta t, t + \Delta t) = f^t(x, t + \Delta t) \tag{2}$$

$$f^t_i(x, t + \Delta t) = f_i(x, t) - \frac{1}{\tau} [f_i(x, t) - f_i^{eq}(x, t)] \tag{3}$$

In the streaming step, fluid particles start to move to neighboring nodes where collision then happens. This can lead the flow system into a dynamic state, that can be revealed on the macroscopic flow behavior until the equilibrium state is achieved in the whole system where equilibrium distribution function $f_i^{eq}(x, t)$ can be defined as Equation (4), in which w_i is the weight of the i th velocity component depending on the selected lattice model, such as D3Q15, D3Q17 and D3Q19 [75,77,78].

$$f_i^{eq} = \omega_i \rho \left[1 + \frac{1}{c_s^2} (e_i \cdot u) + \frac{1}{2c_s^4} (e_i \cdot u)^2 - \frac{1}{2c_s^4} u^2 \right] \tag{4}$$

The most widely used D3Q19 (Figure 8) lattice model for 3D flow simulation is adopted in this study, and the lattice discrete velocity e_i in D3Q19 lattice model is expressed as follows:

$$e_i = \begin{bmatrix} 0 & 1 & -1 & 0 & 0 & 0 & 0 & 1 & 1 & 1 & 1 & 0 & 0 & -1 & -1 & -1 & -1 & 0 & 0 \\ 0 & 0 & 0 & 1 & -1 & 0 & 0 & 1 & -1 & 0 & 0 & 1 & 1 & 1 & -1 & 0 & 0 & -1 & -1 \\ 0 & 0 & 0 & 0 & 0 & 1 & -1 & 0 & 0 & 1 & -1 & 1 & -1 & 0 & 0 & 1 & -1 & 1 & -1 \end{bmatrix} \tag{5}$$

Besides, the weight w_i is designated for $i = 0$, $w_0 = 1/3$, for $i = 1-6$, $w_i = 1/18$, and for $i = 7-18$, $w_i = 1/36$.

In order to adjust use of the LB model to fluid flow in porous media such as rocks in this study, one must incorporate porosity ϵ into the equilibrium equation (Equation (4)), which can be rewritten as Equation (6). Besides, the external force $F_i(x, t)$ in the i th direction of the lattice model is necessarily considered in the LB equation by modifying Equation (1) into Equation (7). $F_i(x, t)$ can be expressed in Equation 8, where F refers to the total external force of a single predetermined lattice node which is predefined manually and I indicates the identity matrix.

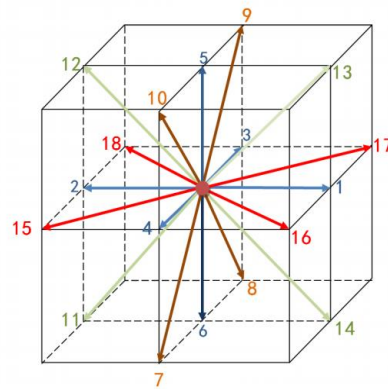


Figure 8. Schematic diagram of D3Q19 model.

$$f_i^{eq}(x, t) = \rho \omega_i \left[1 + \frac{e_i \cdot u}{c_s^2} + \frac{e_i \cdot u}{2\epsilon c_s^4} + \frac{u \cdot u}{2\epsilon c_s^2} \right] \quad (6)$$

$$f_i(x + e_i \Delta t, t + \delta t) - f_i(x, t) = -\frac{1}{\tau} (f_i(x, t) - f_i^{eq}(x, t)) + \Delta t F_i(x, t) \quad (7)$$

$$F_i(x, t) = \rho \omega_i (1 - 0.5\tau) \left[\frac{e_i \cdot F}{c_s^2} + \frac{(F \cdot u) \cdot (e_i \cdot e_i - c_s^2 I)}{2\phi c_s^4} \right] \quad (8)$$

As a result, the macroscopic flow properties such as density, velocity and pressure and can be retrieved through the following equations:

$$\rho = \sum_i f_i(x, t), u = \frac{\sum_i f_i(x, t) e_i}{\rho} + \frac{\Delta t}{2} F, p = \rho c_s^2 \quad (9)$$

Furthermore, the Navier–Stokes equation is recovered through the Chapman–Enskog expansion into the following equation:

$$\frac{\partial \rho}{\partial t} + \nabla \cdot (\rho u) = 0 \quad (10)$$

$$\frac{\partial \rho}{\partial t} + \nabla \cdot (\rho u u) = -\nabla p + \nabla \cdot \left[\rho v \left(\nabla u + (\nabla u)^T \right) \right] + F$$

In the end, the Darcy' law is used to calculate the permeability of rocks:

$$K = -\frac{v \langle u \rangle}{\frac{\Delta p}{L} - F} \quad (11)$$

where K is the permeability, $\langle u \rangle$ is the average velocity of seepage flow system when steady state is realized and $\Delta p/L$ denotes the pressure gradient along the flow direction.

Based on the established porosity-adaptive single-phase LB model above, single-phase flow simulation is run on the 3 REV_s extracted in Section 3.1 and each of these subdomains is discretized into $800 \times 800 \times 400$ lattices, meaning that one voxel in the 3D rock CT image is equivalent to the size of one lattice in the LB model. The fluid density and viscosity are initialized the same as those of CO₂-saturated brine where $\rho = 1100$ kg/m³ and $\nu = 0.0011$ Pa.s, according to [20]. The pressures for inlet and outlet along the flow direction (upward) are set to 100 Pa and 50 Pa, respectively, or differential pressure is 50 Pa. The main idea of this part of work is to extract a tighter REV from these three based on simulated pressure and velocity fields and calculated permeability for each of them, with relevant results shown in the following Section 4.1.

3.3. Multiphase Color LB Model

The multiphase multi-relaxation time (MRT) color LB model, firstly proposed by Gustensen et al. [81], is one of the most popular multiphase LB models [27,62,78] that can

be implemented on complex boundary conditions like pore geometries. In the multiphase color LB model, colors are set to indicate different phases of the flow system where red in general refers to the wetting phase, while the nonwetting phase is indicated by blue.

This work is dependent upon a multiphase color LB model customized for two-phase CO₂–brine flow in rocks, in which separate LB equations are utilized to keep track of the mass transport of each phase and total momentum of both. Unlike the single-phase model, two discrete velocity sets are separately considered for the physical evolution of two phases where the D3Q19 lattice model is adopted for momentum transport LB equations, whereas the mass transport LB equations are dependent upon the D3Q7 model, which is aligned with the first seven discrete velocity components of the D3Q19 lattice model. The densities for both fluid phases, ρ_{nw} and ρ_w (CO₂ and brine in this case), are solved through mass transport LB equations, respectively formulated, and provide essential information on the distribution of two phases and the location of their interface. Under this circumstance, nonwetting or wetting saturation S_{nw} and S_w can be calculated from the densities of both phases and is introduced and expressed in Equation (12):

$$\begin{aligned} S_{nw} &= \frac{\rho_{nw}}{\rho_{nw} + \rho_w} \\ S_w &= \frac{\rho_w}{\rho_{nw} + \rho_w} \end{aligned} \quad (12)$$

Additionally, S_{nw} can also be related to a phase indicator denoted as φ by the following equation:

$$\varphi = 2S_{nw} - 1 \quad (13)$$

Since the maintenance of the two-phase interface is critical to the LB implementation and the diffusion between both fluids is an important mechanism of it, stresses between both phases may occur as a result of interfacial tension and should therefore be incorporated into the momentum transport equation. Logically, the color gradient is defined as follows:

$$\mathbf{C} = \nabla \varphi \quad (14)$$

In typical LB implementations, the color gradient at the interface can be normalized using the following equation:

$$\mathbf{n} = \frac{\mathbf{C}}{|\mathbf{C}|} \quad (15)$$

Additionally, then the D3Q7-based mass transport equations for both phases (wetting and nonwetting) can be established as in Equation (16) based on their momentary densities and velocities until the equilibrium state is matched, where the flux through the interface is minimized and the distributions of both densities and velocities are stabilized.

$$\begin{aligned} g_{nwq} &= \omega_q [\rho_n (1 + \mathbf{e}_q \cdot \mathbf{u}) + \beta (\mathbf{e}_q \cdot \mathbf{n}) \rho_w \rho_n / (\rho_w + \rho_n)] \\ g_{wq} &= \omega_q [\rho_w (1 + \mathbf{e}_q \cdot \mathbf{u}) - \beta (\mathbf{e}_q \cdot \mathbf{n}) \rho_w \rho_n / (\rho_w + \rho_n)] \end{aligned} \quad (16)$$

where β is a parameter controlling the thickness of the interface and g_{nwq} and g_{wq} are defined as the mass transport distribution of nonwetting and wetting phases, respectively, and the weights assigned in the D3Q7 lattice model are $w_0 = 1/3$, for $q = 1 - 6$, $w_q = 1/9$. Besides, the velocities and time evolution of densities for two phases are determined as follows:

$$\begin{aligned} u_i(x, t) &= \frac{\sum_{q=0}^6 g_{iq}(x, t) \cdot e_q}{\rho_i(x, t)} \\ \rho_i(x, t + \Delta t) &= \sum_{q=0}^6 g_{iq}(x - \mathbf{e}_q \Delta t, t) \quad (i = w, nw) \end{aligned} \quad (17)$$

A special reminder is given here that a streaming step is directly applied into the equilibrium distribution functions without relaxation time like in the single-phase LB formulation.

At the same time, the momentum transport equations for both phases are characterized by a D3Q19-based MRT-LB scheme:

$$f_q(x + e_q \Delta t, t + \Delta t) - f_q(x, t) = M_{qi}^{-1} \Lambda_{ii} (m_i^{eq} - m_i) + \omega_q e_q \cdot \frac{F}{c_s^2} \tag{18}$$

where $q, i = 0, 1, 2, 3, \dots, 18$; and the $f_q(x, t)$ is the distribution function of fluid particles, which illustrates the probability that particles at position x travel along the q th direction during the collision step; in the streaming step, $f_q(x + e_q \Delta t, t + \Delta t)$ is the particle evolutionary distribution that measures how a given lattice node x influences the neighboring ones over a time step Δt . In the MRT-LB numerical scheme, Λ_{ii} is designated as a relaxation diagonal matrix (see [5]) governing the relaxation processes of a total of 19 moment components in the D3Q19 lattice structure and is represented as a function of averaged fluid dynamic viscosity ν , which is calculated from those of both non-wetting and wetting phases (Equation (19)). The 19 moment components are determined through a linear transformation: $m_i = M_{qi} f_q$. Meanwhile, the equilibrium moment components denoted as $m_i e_q$ are reliant on the total flow velocity u and color gradient C . Ultimately, the macroscopic total averaged density and velocity for both fluids can be obtained by Equation (20).

$$u = \frac{(1 + \varphi) \nu_{nw}}{2} + \frac{(1 - \varphi) \nu_w}{2} \tag{19}$$

$$\begin{aligned} \rho &= \sum_{q=0}^{18} f_q \\ u &= \frac{\sum_{q=0}^{18} f_q e_q}{\rho} \end{aligned} \tag{20}$$

Moreover, the total fluid pressure p at a given position is calculated from sound speed and total density denoted, given as c_s ($c_s = 1/\sqrt{3}$) and ρ , respectively, using the formula $p = \rho c_s^2$.

The non-equilibrium moment components of 19 in total are the following ones:

$$\begin{aligned} m_1^{eq} &= (j_x^2 + j_y^2 + j_z^2) + \alpha |C| \\ m_9^{eq} &= (2j_x^2 - j_y^2 + j_z^2) + \alpha \frac{|C|}{2} (2n_x^2 - n_y^2 - n_z^2) \\ m_{11}^{eq} &= (j_y^2 - j_z^2) + \alpha \frac{|C|}{2} (n_y^2 - n_z^2) \\ m_{13}^{eq} &= j_z j_y + \alpha \frac{|C|}{2} n_z n_y \\ m_{14}^{eq} &= j_x j_y + \alpha \frac{|C|}{2} n_x n_y \\ m_{15}^{eq} &= j_x j_z + \alpha \frac{|C|}{2} n_x n_z \end{aligned} \tag{21}$$

where j_x, j_y, j_z represent the magnitude of components of the total momentum j ($j = \rho u$) along three coordinate axes: x, y, z under Cartesian coordinate system and similarly n_x, n_y and n_z are three components along them as to the normalized color gradient n . α is linearly related to interfacial tension between two phases: $\sigma_{nw}, n = 6\alpha$. For further information on the concrete formulations of M_{qi}, m_i^{eq} and Λ_{ii} , please refer to the literature, including but not limited to [5,74,81].

3.4. Two-Phase Flow Parameters and Steady-State LBPM

Relative permeability is the most critical macroscopic flow parameter for two-phase flow in porous media, being a good indication of the flow capacity of either fluid in the multiphase scenarios compared with the single-phase one. Factors controlling it include many rock and fluid properties that can be summarized by nondimensional parameters.

Nondimensional flow parameters including capillary number (Ca), viscosity ratio (M) and wettability index (WI), being the first-order or most important ones, play a highly critical role in two-phase flow regimes in complex pore geometries as boundary conditions and therefore have an indispensable impact on macroscopic flow properties like fluid pressure and velocity, ultimately resulting in variation of relative permeability of both nonwetting and wetting fluids.

Regarding multiphase flow in porous media, a multiphase expansion of Darcy's law (Equation (11)) is widely used to characterize two-phase CO_2 -brine flow in rocks at reservoir scale. The wetting phase has a stronger affinity to the rock surfaces than nonwetting phase, resulting in the emergence of different flow patterns between them due to thermodynamics. As such, the competitive passage of both fluids through the rocks occurs and the two-phase modified Darcy's law is constructed to interpret this effect, as in the following equation:

$$u_i = -\frac{k_{ri}}{\nu_i} K(\nabla p - \rho_i g) \quad (22)$$

where u_i ($i = nw, w$) is the velocity of the nonwetting or wetting fluid phase; k_{ri} refers to the relative permeability of both phases; ν_i indicates their dynamic viscosities and K is the absolute permeability of the rock sample. In addition, ∇p and $\rho_i g$ hereby symbolize pressure gradient along the flow direction, as in the traditional Darcy's law and the body force of the nonwetting or wetting phase, which is also part of external force applied into the flow system.

Wettability makes a great contribution to the fluid distribution, fluid–fluid interaction and flow pattern in the pore space. It is a good measure of the tendency of either fluid of both phases to compete to stick to and spread across the rock surface. Contact angle θ can be measured at the liquid–solid contact interface in the experiments as shown in Figure 9 and calculated from interfacial tension $\sigma_{nw,n}$ and surface tensions for both fluids ($\sigma_{nw,s}$ and $\sigma_{w,s}$) based on the Young's equation [67], as in Equation (23):

$$\cos \theta = \frac{\sigma_{w,s} - \sigma_{nw,s}}{\sigma_{nw,n}} \quad (23)$$

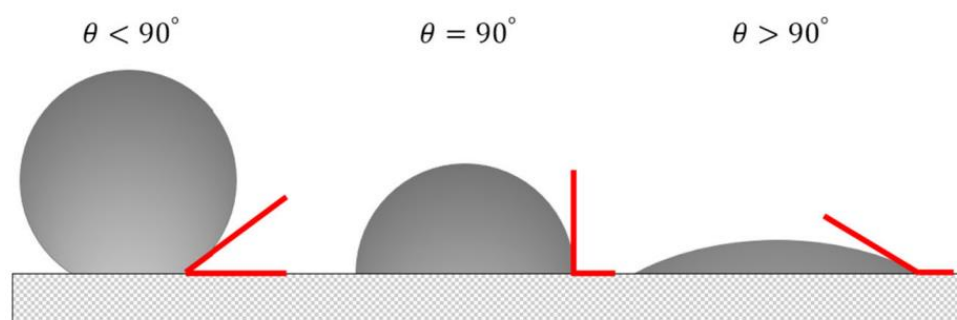


Figure 9. Schematic diagram showing the contact angle where a fluid droplet drops onto the rock surface [5].

Therefore, WI can be expressed by the cosine of the contact angle at the rock–fluid interface, which lies in the range between -1 and 1 . By referencing [82], wetting conditions for the CO_2 -brine-sandstone fluid–fluid–solid system in this paper are defined as the following criteria based on WI : $WI = 1$ or -1 represents the fact that the whole rock system is either completely water-wet or CO_2 -wet; it is strongly water-wet when WI is between 0.8 and 1 , whilst strongly CO_2 -wet for -1 to 0.8 ; intermediately water-wet for 0.5 to 0.8 and intermediately CO_2 -wet for -0.8 to -0.5 ; weakly water-wet for 0 to 0.5 and weakly CO_2 -wet for -0.5 to 0 . Since extreme cases, such as being completely water or CO_2 -wet, are seldom seen in real reservoir conditions, most of which, additionally, are water-wet to

various extents, therefore only the effects of strongly water-wet, intermediately water-wet, and weakly water-wet scenarios are reported in this paper.

Capillary number or Ca is another essential nondimensional flow parameter that characterizes the domination between viscous and capillary forces in the flow behavior of both phases. It can be defined as the ratio of viscous force and capillary force. The viscous force dominates the flow pattern and enhances the mobility of both wetting and nonwetting fluids at high Ca . On the contrary, when it comes to a low capillary number, which means that there is a more competitive effect of capillary force over the flow system than that of the viscous force, both two phases will reduce their movable contents and be blocked into some local space because of the capillary resistance effect. The formula expressing the capillary number Ca is the following one:

$$Ca = \frac{\nu_{nw} \mathbf{u}}{\sigma_{nw,w}} \quad (24)$$

where ν_{nw} is the dynamic viscosity of the nonwetting phase; \mathbf{u} is the total velocity and $\sigma_{nw,w}$ is the interfacial tension between two phases.

The viscosity ratio M is the third important controlling factor, except for the two other aforementioned ones for two-phase flow in porous media, and is defined as the ratio of dynamic viscosities between wetting and nonwetting phases as shown in Equation (25). Additionally, its importance level with respect to flow regimes in the pore space is dependent on the capillary number, where at high capillary number ($Ca > 10^{-4}$, e.g.), the viscosity ratio has a significant impact on the results, and the smaller contrast is between the viscosities of the two phases, the more favorable flow is for both of them; whereas, there is little or no effect on their flow patterns at low capillary number ($Ca < 10^{-4}$, e.g.), since under this condition either wetting or nonwetting phase is blocked due to the capillary effect [5,28,34,82].

$$M = \frac{\nu_w}{\nu_{nw}} \quad (25)$$

The LB method is one of the most suitable numerical methods for digital rock physics represented by multiphase flow processes in rocks, and is used to efficiently deal with complex boundary conditions as pore geometries without losing its characteristics. Meanwhile, it is a mesoscopic method that contains micro-scale physical mechanisms and relates them to nondimensional parameters. For example, local surface wettability can be initialized based on laws accounting for non-equilibrium and equilibrium effects [5,82]. In general cases, the color LB model is the most widely used LB model in simulating immiscible two-phase fluid flow in complex porous media and stays stable for running over a wide range of nondimensional parameters: $10^{-6} < Ca < 1$; $0.01 < M < 100$ and, the model is adept at coping with the cases with big density contrast (larger than 100 between two phases).

Experiments for steady-state two-phase flow in rocks are popular for measuring relative permeability in the laboratory by monitoring the pressure drop along the rock sample at a given saturation of one fluid. However, such experiments fail to create rigorous steady-state flow due to spontaneous uncertainties in the fluid saturation [25]. By contrast, LB numerical simulations show uncompetitive strengths by imposing a periodic boundary at both inlet and outlet to secure a constant saturation of one fluid. A color LB model based on the use of digital rock images to simulate the steady-state two-phase flow in porous media is proposed by [5] and is also called steady-state LBPM (lattice Boltzmann models for porous media). Simply put, the successful implementation on the steady-state LBPM relies on two components: 1. a mechanism to drive and supervise the flow pattern of fluids at a constant saturation 2. a mechanism to evolve the flow configuration with changing the target saturation. Notably, during the steady-state LBPM simulation of CO₂-brine immiscible flow in digital rock images, both phases are initialized at a target saturation based on morphology adaption [5,28] in the pore space, and the CO₂ as the nonwetting phase is typically assigned in the large pores.

In this paper, a tighter $200 \times 200 \times 200$ voxels REV (Figure 10a) with porosity and permeability of, respectively, 8.45% and 16.52 mD, was extracted at the center of REV1 (Figure 10b), and this was significantly less permeable than other the two as demonstrated in the previous part. To follow up, the steady-state LBPM is used to simulate two-phase CO_2 –brine immiscible flow in this tighter REV to study effects of nondimensional parameters on relative permeability with optimized differential pressure, after which we discussed flow pattern and capacity of CO_2 under different cases and gave insights into CO_2 storage efficiency based on estimated CO_2 residual saturation ($S_{\text{residualCO}_2}$) as discussed in Section 4.3.

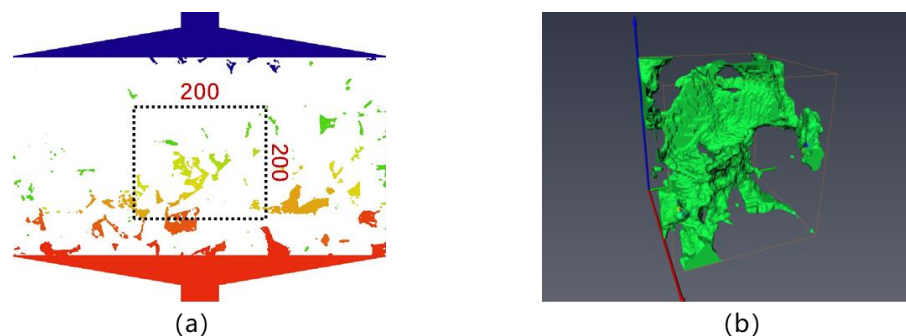


Figure 10. Cross section of the pressure field of REV1 with a square bounded by black dash lines, indicating the scope of a tighter $200 \times 200 \times 200$ voxels REV to be extracted (a) and the pore structure (b) of it denoted in green bounded by a cube as the computational domain.

4. Results and Discussions

4.1. Single-Phase LB Simulation and Extraction of Tighter REV

Single-phase LB simulations on three REV_s (REV1, REV2 and REV3), extracted from the whole-core digital rock image of the rock sample, were conducted based on the model initial inputs as illustrated in Section 3.2 of this paper. Calculated permeabilities of three REV_s are 50 mD, 532 mD and 900 mD, seeing big contrast between each other, despite originating from the same macroscopically permeable sandstone core sample. Besides, pressure (Figure 11a–c) and velocity fields (Figure 11d–e) were also visualized after the simulations, which shows that REV1 is remarkably more abnormal than the other two ones where no significant pressure drop is observed in the pressure field and discontinuous streamlines exist across the global domain, with extremely low flow velocity near zero at the outlet. The pressures and velocities are converted into the dimensionless form by dividing the value of a simulated sample at one certain position by the maximum value within the computational domain as the characteristic value under all the scenarios.

Based on the permeability calculations and results from the physical (pressure, velocity) fields of these three REV_s, we suggest using a local domain inside REV1 with low permeability to account for the simulation results on the global-field scale. From this point of view, we determined to cut a tighter REV at the center of REV1 with a size of $200 \times 200 \times 200$ voxels from which pore structure is characterized in Figure 10b. Figure 10a points out the cross section of the tighter $200 \times 200 \times 200$ voxels REV extracted at the center of REV1. What can be seen from its pore structure shown in Figure 10b is that plane porosities on bounded facets of the cubic computational domain are limited and that only one connected pore–throat system is across the microstructure. It is then speculated that poor injectivity of fluids into the tighter pore space may cause complicated two-phase CO_2 –brine flow behavior in it, which directly has an impact on CO_2 storage efficiency. Furthermore, we surmise that the effect of this kind of micro-scale CO_2 storage mechanism may be upscaled in many of permeable deep saline sandstone aquifers at core scale or even reservoir scale. Based on this inference, a series of simulations of two-phase CO_2 –brine flow in this tighter REV under different circumstances including various differential pressures and combinations of nondimensional parameters introduced above using the steady-state

LBPM. Based on the simulated results obtained under these scenarios, some insights are given into the CO₂ storage efficiency in this microstructure.

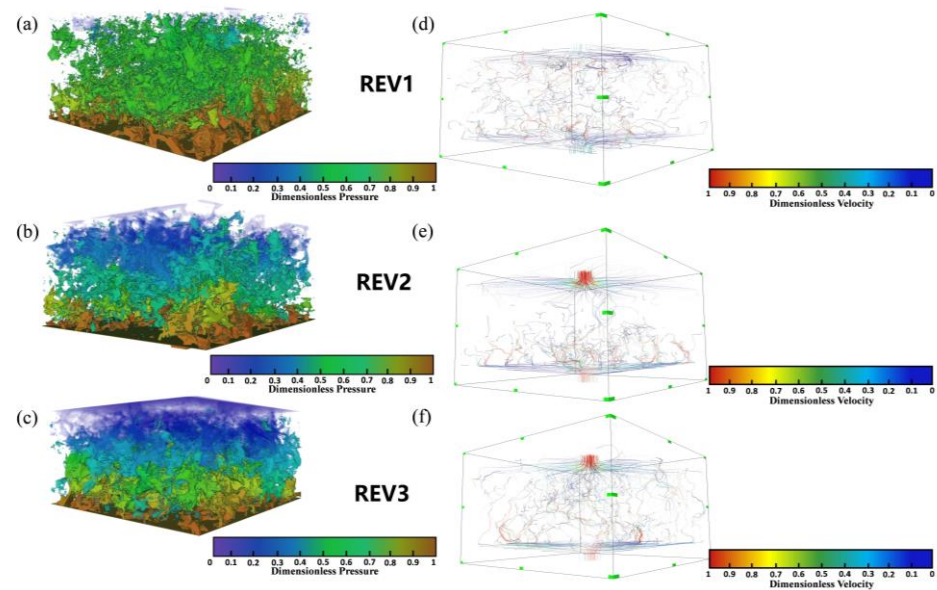


Figure 11. Pressure (a–c) and velocity (d–f) distributions of REV1, REV2 and REV3, two parameters are presented in the dimensionless form ranging from 0 to 1, aiming to illustrate the big contrast.

4.2. Threshold Pressure Gradient and Optimization of Differential Pressure

There exists nearly zero-velocity non-Darcy flow in porous media with low permeability or pore connectivity under a certain pressure gradient across the flow domain which is called as threshold pressure gradient. Besides, non-Darcy low-velocity flow features another interval between the threshold pressure gradient and a point from which the Darcy flow starts [68]. Threshold pressure gradient plays an important role in flow behaviors in ultra-tight reservoirs at the macroscopic scale, which is correlated with many engineering applications such as enhanced oil recovery, ground water discharge and natural gas or hydrate production in these types of reservoirs [68,69]. However, so few reports in the literature were made on the micro-scale effects of threshold pressure gradient on two-phase CO₂–brine flow in tight sandstone pore structures. In this section, a couple of LB simulations of two-phase CO₂–brine flow in the tighter 200 × 200 × 200 voxels REV were conducted with 4 differential pressures, P_{diff} : 100 Pa, 200 Pa, 300 Pa and 400 Pa, and their pressure gradients were converted to 0.25 MPa/m, 0.5 MPa/m, 0.75 MPa/m, 1 MPa/m in order to see if threshold pressure gradient exists in the tighter REV and select the optimized differential pressure where two-phase flow has been fully channelized through the pore structure, characterized by stable and nearly equal flow rate at both inlet and outlet and continuous pressure drop along the flow direction, as typical of the Darcy flow. The reason for the parametric selection was based on the literature [69–71], where most of threshold pressure gradient values that are measured in core flooding experiments lie between 0.005 MPa/m and 1.5 MPa/m at the core scale.

Initializations for the steady-state LBPM include the following components: wettability index WI on the rock surface is set to be 0.7, which is typical of intermediately water-wet conditions; viscosity ratio between two phases is 10 where ν_{nw} and ν_w are 1×10^{-7} Pa.s and 1×10^{-6} Pa.s (CO₂ is the nonwetting phase and brine is the wetting phase); density for CO₂ ρ_{CO_2} is 1000 kg/m³ at the supercritical state and brine density ρ_{Brine} is designated at 1100 kg/m³ when CO₂ is saturated; capillary number Ca in this part is defined as 1×10^{-4} ; the tighter REV is saturated with brine and CO₂ at equal fractions: S_{CO_2} and S_{Brine} are the same as 50%;

Figure 12a–d are simulated results of flow velocity distribution within the domain of tighter REV under the above 4 scenarios of various differential pressures (100 Pa, 200 Pa, 300 Pa, 400 Pa), likewise, the velocity here is converted to the dimensionless form as Figure 11 by dividing the value at any position by characteristic velocity—the greatest value encountered under four runs. These results indicate that for $P_{diff} = 100$ Pa (Figure 12a), there is nearly no fluid motion in the whole global domain, symbolizing that the flow system in this scenario is immobilized due to its differential pressure below the threshold one. Flow velocity localization was observed at the inlet when P_{diff} reached 200 Pa (Figure 12b), which demonstrates that so few parts of fluid near the entrance under this circumstance have been activated, and the whole computational domain is not yet fully channelized. We therefore assume that the threshold pressure gradients that are frequently encountered in macroscopic experimental investigations also exists at a microscopic scale like in this study, where threshold pressure gradient is in the vicinity of 0.5 MPa/m, which matches some of the experimental results reported in the literature [55–57]. Besides, it is notable in Figure 12c that the flow was fully channelized under $P_{diff} = 300$ Pa and has approximately conformed to Darcy flow behaviors. This discovery can further imply that the linear Darcy flow was realized at a differential pressure P_0 equal to or below $P_{diff} = 300$ Pa, and that non-Darcy flow dominated the flow regime in the computational domain when the P_{diff} lied in the interval between around 200 Pa and P_0 . Intuitively, the case with $P_{diff} = 400$ Pa (Figure 12d) can give further proof that flow is not only channelized and flow rates at both sides are closer than $P_{diff} = 300$ Pa. Figure 13 represents the pressure profiles of 4 scenarios with different pressures, from which one can tell that pressure profile keeps nearly constant along the flow direction, accompanied by a drastic plunge in the near-outlet region when differential pressure is 100 Pa and 200 Pa, in sharp contrast to which, significant and continuous pressure drop is observed at $P_{diff} = 300$ Pa and 400 Pa, where the flow has been fully channelized, a typical characteristic of the Darcy flow behaviors; in addition, the linearity of pressure profile gets stronger as P_{diff} evolves from 300 Pa to 400 Pa. Based on the demonstrated research results on the pressure profile of the tighter REV under 4 differential pressures, a couple of our insights are given as follows. Variation of pressure distribution along the flow direction in the non-Darcy flow interval (revealed by Figure 13b) and when differential pressure is lower than the threshold pressure (revealed by Figure 13a) is small, based on which we suggest that most of the fluid confined in the pore space can hardly be mobilized under the current differential pressure by overcoming the capillary resistance while the scope of pressure propagation covers the computational domain by equalizing the pressure distribution in it. Besides, the sharp plunge near the end is attributed to pressure continuity between predefined pressures at inlet and outlet from our humble perspective. Moreover, a pressure drop is significantly revealed with stronger linearity, especially as differential pressure gets larger after fluid flow enters the Darcy flow state (Figure 13c,d).

In summary, optimized differential pressure of 400 Pa was selected, at which flow is fully channelized with stably similar flow rates at both inlet and outlet and nearly linear pressure drop is established for the following simulations regarding sensitivity analysis for relative permeability under various combinations of nondimensional parameters in the following part of this paper.

4.3. CO₂ Relative Permeability and Storage Efficiency

The two-phase CO₂–brine imbibition processes are of great research significance to CO₂ storage efficiency in pore spaces of sandstone reservoirs. As discussed before, most of pore surfaces in deep saline aquifers are water-wet to varying degrees. As such, in this section, the steady-state LBPM was utilized to simulate the CO₂–brine imbibition processes over a range of target saturations (0.2–0.9) under a total of 18 scenarios (Table 1) constituting different combinations of 3 nondimensional parameters (Ca , M , WI) using the optimized differential pressure (400 Pa), with the highest injectivity of brine in the tighter REV in order to validate the systematic effects of nondimensional parameters on relative permeability for

CO₂ as the nonwetting phase and therefore discuss CO₂ storage efficiency as the residual phase in the pore geometry under these 18 cases (Table 1).

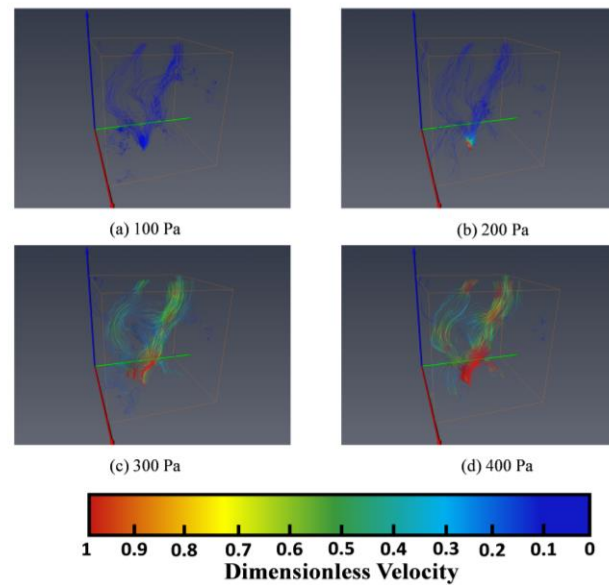


Figure 12. Velocity distributions of two-phase flow (nonwetting phase–CO₂, wetting phase–brine) in the tighter REV when P_{diff} is equal to 100 Pa (a), 200 Pa (b), 300 Pa (c), 400 Pa (d) at $S_{CO_2} = 0.5$, $Ca = 1 \times 10^{-4}$, $M = 10$ and $WI = 0.7$.

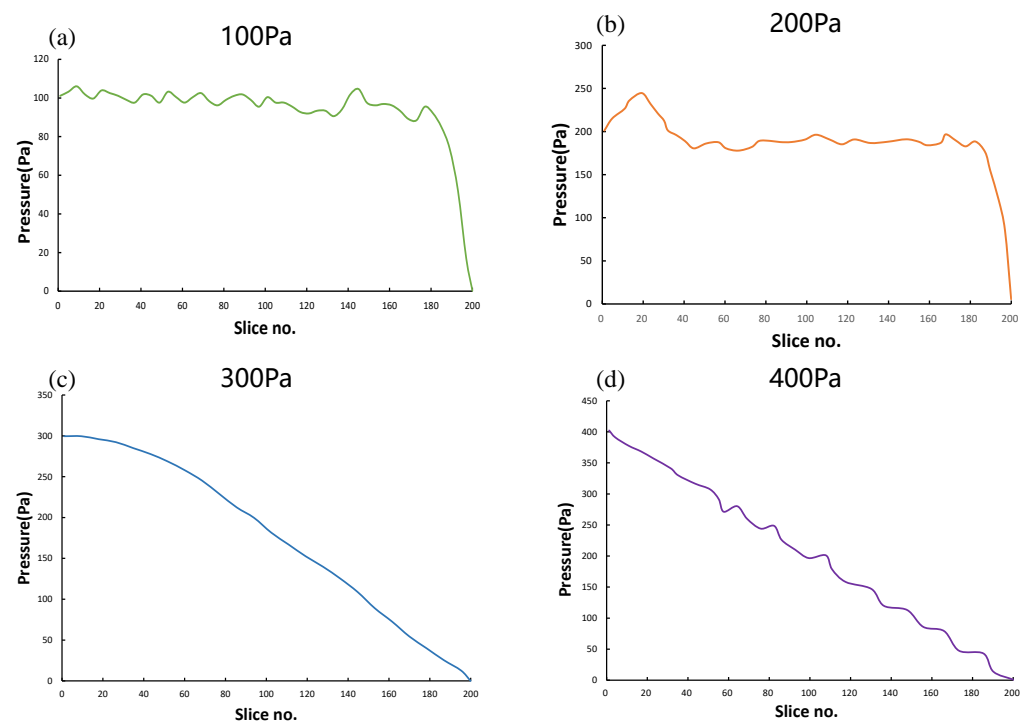


Figure 13. Pressure profiles of the tighter REV versus CT slice when steady state is reached as P_{diff} is equal to 100 Pa (a), 200 Pa (b), 300 Pa (c), 400 Pa (d) with the same initial conditions as Figure 12.

Table 1. All 18 scenarios constituting different combinations of three nondimensional parameters (capillary number (Ca), viscosity ratio (M) and wettability (WI)) for two-phase CO₂–brine imbibition processes.

Scenario No.	Capillary Number (Ca)	Viscosity Ratio (M)	Wettability (WI)
1	1×10^{-3}	1	0.3
2	1×10^{-4}	1	0.3
3	1×10^{-5}	1	0.3
4	1×10^{-3}	1	0.7
5	1×10^{-4}	1	0.7
6	1×10^{-5}	1	0.7
7	1×10^{-3}	1	0.9
8	1×10^{-4}	1	0.9
9	1×10^{-5}	1	0.9
10	1×10^{-3}	10	0.3
11	1×10^{-4}	10	0.3
12	1×10^{-5}	10	0.3
13	1×10^{-3}	10	0.7
14	1×10^{-4}	10	0.7
15	1×10^{-5}	10	0.7
16	1×10^{-3}	10	0.9
17	1×10^{-4}	10	0.9
18	1×10^{-5}	10	0.9

In fact, the use of the steady-state LBPM to precisely and physically predict the CO₂–brine imbibition processes, which are naturally unsteady flooding processes, requires an initialized fluid distribution where CO₂ almost saturates the whole porosity and the near-inlet region is filled up with brine, as illustrated in Figure 14b, followed by simulations of CO₂–brine imbibition processes over a span of target saturations. A better visualized example of the process is presented in Figure 15, from which one can easily see that model initial conditions match scenario 14 at Table 1. Results from Figure 15 show that the wetting-phase breakthrough happened along with brine rapidly dominating the main connected channel in the pore space until the global fluid distribution and flow pattern was stabilized as the target saturation reached a certain level, like $S_{Brine} = 0.5$ in this case, where relative permeability of CO₂ nearly approached zero and it was expelled into isolated big pores and stored as residual phase.

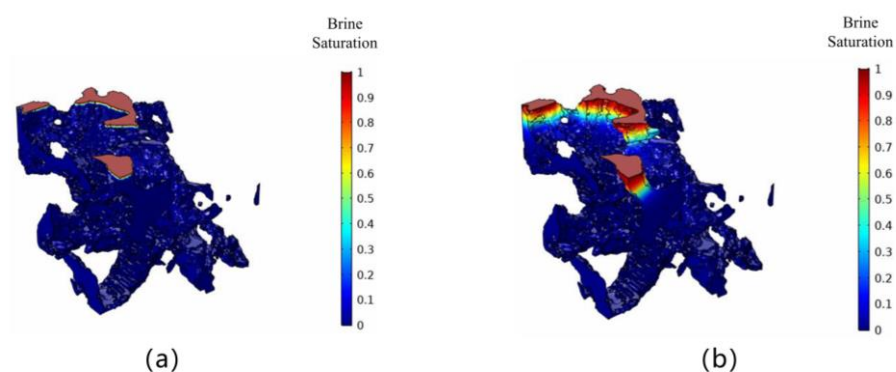


Figure 14. The tighter REV saturated with CO₂ (a) was initially saturated with brine in the near-inlet region with global target brine saturation of 0.05, (b) as prepared for the CO₂–brine imbibition process over a range of target saturation from 0.2 to 0.9 with initial model conditions the same as in Section 4.2.

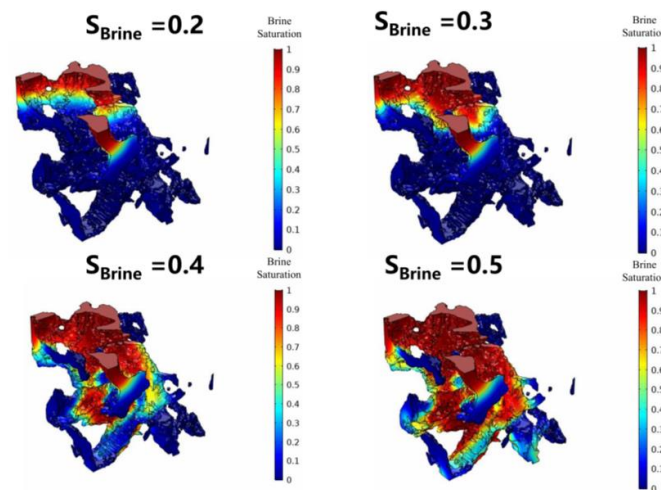


Figure 15. Steady-state brine distribution of the tighter REV, during the CO₂–brine imbibition process over a range of target saturation from 0.2 to 0.5., the flow pattern and fluid distribution are stabilized when the global target saturation reaches 0.5 where the flow is channelized and dominated by brine.

Figure 16 shows simulated relative permeability curves for CO₂ (nonwetting) over a span of target saturations ranging from 0.2 to 0.9 under a total of 18 scenarios constituting various combinations of three nondimensional parameters. As a result, a systematic interpretation of effects of these three parameters on relative permeability of CO₂ is made, followed by CO₂ storage efficiency analysis based on these simulated relative permeability curves through setting up a lower bound ($k_{rCO_2} = 0.05$), below which the ability of CO₂ to leave the pore space is infinitely small and can be assumed as zero. Here, in this study, the brine saturation at which the CO₂ relative permeability firstly drops below 0.05 is denoted as $S_{Brine\max}$. The approximated CO₂ residual saturation ($S_{residualCO_2}$) is therefore calculated by the following equation:

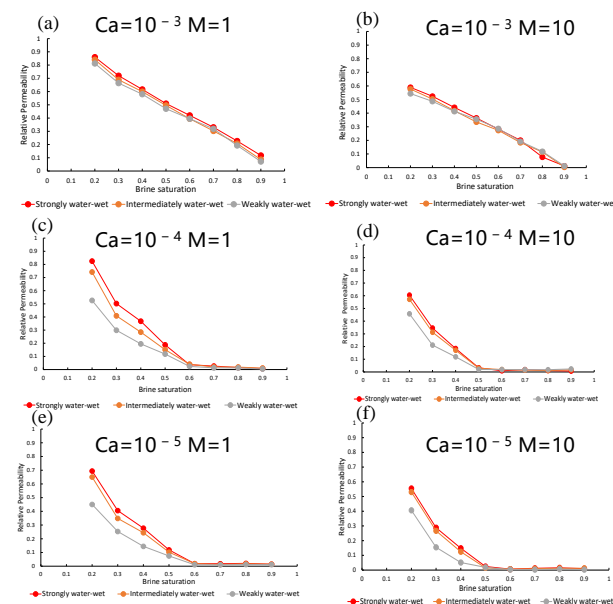


Figure 16. Simulated relative permeability curves for CO₂ (nonwetting) under the total 18 scenarios, with different combinations of three nondimensional parameters including capillary number (Ca), wettability index (WI) and viscosity ratio (M) described in Table 1. $WI = 0.3$, $WI = 0.7$ and $WI = 0.9$ respectively weakly water-wet, intermediately water-wet, and strongly water-wet. (Note: (a) and (b) represent cases under high capillary number ($Ca = 1 \times 10^{-3}$), while those under low capillary numbers ($Ca = 1 \times 10^{-4}$, $Ca = 1 \times 10^{-5}$) are done by (c–f).)

$$S_{residualCO_2} = 1 - S_{Brinemax} \quad (26)$$

As we discussed in the previous sections, capillary number is divided into high or low values based on a boundary value in between, and it is clear from Figure 16 that simulation results at $Ca = 1 \times 10^{-5}$ and 1×10^{-4} are not considerably distinguishable without varying the other two parameters. By contrast, relative permeability for CO_2 is significantly higher at $Ca = 1 \times 10^{-3}$, when other conditions are controlled. This obvious comparison can validate the fact that the boundary value of Ca for our study is equal to 1×10^{-4} or lower but much higher than 1×10^{-3} , beyond which capillary effect is enough to confine CO_2 as nonwetting phase in the pores, especially larger ones, and further effects are obscure with increasing Ca . Additionally, the linearity for relative permeability of CO_2 in the case with $Ca = 1 \times 10^{-3}$ is much stronger than those with $Ca = 1 \times 10^{-4}$ or 1×10^{-5} when $M = 1$, which illustrates that the flow of CO_2 at low capillary number is totally dominated by the viscous force; besides, if possibly M is low enough as 1, like in Figure 16a, the CO_2 flow pattern is much closer to characteristics of Poiseuille flow than other scenarios, given that brine spreads across the rocks surface as a water film that facilitates the flow of CO_2 . Nevertheless, the viscosity ratio also plays a crucial role in varying CO_2 relative permeabilities at both high and low capillary numbers. A comparison of Figures 16a and 16b offers us an essential piece of information that the slope or the rate of the decline of CO_2 relative permeability curves is lower at higher M than at lower the one, while the overall relative permeabilities over the whole saturation range rise to some degree as M decreases, which is mainly caused, in our view, by the lubrication effect where the water film coating the rock surface shares similar viscosity to CO_2 so that the viscous coupling effect is less apparent. However, at low a capillary number ($Ca = 1 \times 10^{-4}$, $Ca = 1 \times 10^{-5}$), as illustrated from Figure 16c,d, relative permeabilities are only affected by M for the initial saturation range in which the curves have yet to converge to zero, which means that because of the strong dominance of pore confinement at a low capillary number, the effect of viscosity ratio is hereby limited, with only the convergence rate being alleviated by a finite quantity. Finally, the effect of wettability on the relative permeability performance of CO_2 is also discussed in both high- and low-capillary number scenarios, with M being either 1 or 10. Figures 16a and 16b present that relative permeability of CO_2 is insensitive to wettability of the rock surface at high capillary number since viscous force is the dominating force controlling the migration of fluids and the capillary force poses little or no resistance to the nonwetting phase flow. Moreover, the capillary force plays an essential role in manipulating the flow system at low capillary, therefore, the effect of wettability on CO_2 relative permeability number seems to be magnified. It is suggested from Figure 16c–f that CO_2 relative permeability is reduced with water-wetting conditions being weaker and that the effect is much more conspicuous when it transforms from intermediately water-wet to weakly water-wet; as brine saturation rises, the wettability effect is also reduced until none. To the best of our knowledge, residual CO_2 is expelled to the larger pores coated by brine and the main porosity is channelized for brine transport through the porous media, with the global target saturation of brine approaching the maximum where no CO_2 in the pores can further be pulled out of the computational domain.

The relative permeability of CO_2 exerts a great impact on its storage efficiency, as illustrated in the literature, and the higher amount of ultimate safe storage capacity, which is presented as the residual phase in the pore space after the two-phase imbibition processes, means higher storage efficiency at relatively lower risk of leakage. In the rest of the paper, we attempt to analyze CO_2 storage efficiency in different scenarios with varying combinations of nondimensional parameters in the tighter REV based on the relative permeability curves of CO_2 by means of setting a lower bound value of 0.05 and identifying the target brine saturation with relative permeability that first breaks down the bound, denoted as the maximum brine saturation $S_{Brinemax}$, which logically derives the CO_2 residual saturation $S_{residualCO_2}$ as expressed in Equation (26). Figure 17 gives a close-up view of relative permeability curves simulated in Figure 17 by narrowing down the brine

saturation scope, where relative permeability values are generally below or approach the lower bound value as illustrated in each panel. Apparently, residual CO_2 saturations are quite distinguishable between cases at high Ca (Figure 17a,b) and at low Ca (Figure 17c,d). One can easily observe that Figures 17a and 17b both demonstrate much less residual saturation of CO_2 than other ones. Estimated CO_2 residual saturations are between 0.1 and 0.2 for $Ca = 1 \times 10^{-3}$, $M = 10$ and 0 and 0.1 for $Ca = 1 \times 10^{-3}$, $M = 1$, respectively, with relative smaller differences. However, at low Ca , all the cases have obviously lower CO_2 residual saturation, with one estimated between 0.5 and 0.6 for $Ca = 1 \times 10^{-4}$ and 1×10^{-5} , $M = 10$ and one between 0.4 and 0.5 for $Ca = 1 \times 10^{-4}$ and 1×10^{-5} , $M = 1$. Based on our analysis, since the whole computational domain is controlled by viscous force with rather less pore confinement effect on the flow of fluids at high Ca than low Ca , the flow of CO_2 is much more favored with less residual CO_2 left in the pores. Consequently, we can primarily conclude that capillary number has an essential role to play in deciding the CO_2 storage efficiency of the two-phase CO_2 -brine flow system as Ca transcends the boundary between low and high Ca values or vice versa, or simply put, higher Ca results in lower CO_2 storage efficiency. When the capillary number is controlled at low values ($Ca = 1 \times 10^{-4}$, 1×10^{-5}), the viscosity ratio seems to influence the CO_2 storage efficiency to some degree. Figures 17b, 17d and 17f present higher CO_2 residual saturation with increasing M from 1 to 10, which suggests that decreased similarity in viscosity between CO_2 and brine leads to a slight improvement in CO_2 storage efficiency due to the mitigated lubrication effect. However, its effect is much less superior to capillary number, for which the pore confinement is responsible. Additionally, it is seen from Figure 17a–f that wettability poses no great changes to the ultimate estimated CO_2 residual saturation when the other two parameters, Ca and M , are constant. Accordingly, we assert that the extent of water-wetting conditions of sandstone rock surfaces is less sensitive to CO_2 storage efficiency, while it only exerts a somehow measurable influence on the CO_2 relative permeabilities before the curves converge to zero at low Ca .

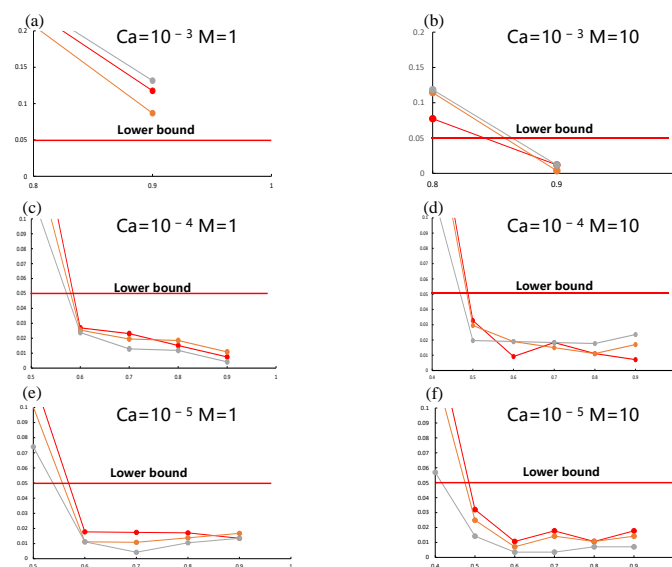


Figure 17. A close-up view of CO_2 relative permeability curves under 18 scenarios at Table 1 by narrowing the scope of brine saturation within which most of the values have fallen into the scale of 0.1. A lower bound value of $k_{r\text{CO}_2} = 0.05$, as the minimum value for assuming the flow of CO_2 through the computational domain is present, is defined; therefore, brine saturations at which the CO_2 relative permeability firstly falls below the 0.05 are considered approximate maximum brine saturation ($S_{\text{Brine max}}$) in the computational domain where CO_2 residual saturation ($S_{\text{residual CO}_2}$) is consequently estimated using Equation (26). (Note: (a) and (b) represent cases under high capillary number ($Ca = 1 \times 10^{-3}$), while those under low capillary numbers ($Ca = 1 \times 10^{-4}$, $Ca = 1 \times 10^{-5}$) are done by (c–f).)

5. Conclusions

In this study, we used the steady-state multiphase color–gradient lattice Boltzmann (LB) model to simulate two-phase CO₂–brine flow in a tight rock image volume (REV) extracted from a digital rock image of a whole-core permeable sandstone under four differential pressures (100 Pa, 200 Pa, 300 Pa, and 400 Pa). We identified a threshold pressure gradient less than or equal to 0.5 MPa/m (200 Pa), a non-Darcy flow interval between 200 Pa and a value smaller than 300 Pa, and Darcy flow behavior at $P_{diff} = 300$ Pa and 400 Pa. The channelization of fluids was observed to improve as the differential pressure increased, with closer flow rates at the inlet and outlet. Pressure profiles along the flow direction were presented for the four differential pressures, demonstrating that the immobilized case ($P_{diff} = 100$ Pa) and non-Darcy flow case ($P_{diff} = 200$ Pa) both exhibited nearly constant pressure distributions, with an abrupt drop only seen near the outlet. In contrast, the Darcy flow interval showed a continuous and significant pressure drop across the domain, and the linearity of the pressure drop increased as the differential pressure increased from 300 Pa to 400 Pa. Based on these findings, we posit that differential pressure is a key factor influencing CO₂–brine flow behavior in the tight REV, with a threshold pressure gradient. The more significant pressure drops and flow channelization in the REV, the more optimized the differential pressure under which the domain is governed by Darcy flow behavior will be. Therefore, $P_{diff} = 400$ Pa was selected for the subsequent two-phase CO₂–brine imbibition process over a range of target saturations in the tight REV.

Furthermore, LB simulations of CO₂–brine imbibition processes over a predetermined range of target saturations under the optimized differential pressure (400 Pa) were conducted in the tight REV under a series of scenarios comprising 18 different combinations of nondimensional parameters (Ca , M and WI). These simulations were carried out in order to understand the dependencies of CO₂ relative permeability and to analyze storage efficiency, as indicated by the estimated CO₂ residual saturation in the pore space. A lower bound of $k_{rCO_2} = 0.05$ was applied to the simulated relative permeability curves. The conclusions in this regard were made based on the simulation results as follows:

1. When examining the effect of the capillary number (Ca) on CO₂ relative permeability, it can be divided into high and low values. At high Ca , the CO₂ relative permeability is globally higher and the relative permeability curve of CO₂ is more linear, resulting in less restricted CO₂ flow across the computational domain due to weaker pore confinement. This leads to significantly lower CO₂ storage efficiency, as indicated by extremely smaller estimates of CO₂ residual saturation compared to those at low Ca .
2. The viscosity ratio (M) is another parameter that influences CO₂ relative permeability and facilitates CO₂ flow in the pore space through the lubrication effect as it decreases. Lower M leads to more favorable CO₂ flow in the imbibition process and thus less residual CO₂ in the pores when other conditions are controlled, implying a negative impact on storage efficiency. However, the impact of the viscosity ratio on relative permeability is significantly less than that of the capillary number. At low capillary number, the lubrication effect is overpowered by the pore confinement effect in the relative permeability curves, while at high capillary number, the reduced viscosity contrast between the two phases may result in a finite improvement in CO₂ flow capacity and lower storage efficiency. However, this difference is not considerably observable because the viscous force in the pores, already dominant compared to the capillary force, masks it.
3. Wettability only affects CO₂ relative permeabilities in the initial saturation range before the curves converge to zero. Under stronger water-wet conditions, CO₂ has an easier time passing through the domain due to less affinity to the surface, but its storage efficiency is relatively insensitive to changes in wettability when other conditions are controlled.

The systematic quantification of CO₂ storage efficiency in a tighter REV in a permeable and heterogeneous sandstone rock sample gives micro-scale insights into how

the mechanisms of two-phase CO₂–brine imbibition processes relate to in situ stable CO₂ storage.

6. Limitations and Expectations

This study has used the steady-state multiphase color–gradient LB model to investigate the effect of various nondimensional parameters on CO₂ storage efficiency, as indicated by CO₂ residual saturation, in a tighter REV with a threshold pressure gradient at the micro scale during the two-phase CO₂–brine imbibition processes. While some new findings have been obtained, there is still room for improvement in both the LB numerical model and the physics of two-phase CO₂–brine seepage flow itself. Some potential avenues for future work include: (1) the development of unsteady-state LB models that consider temporal effects to examine the dynamics of two-phase CO₂–brine seepage flow over the continuous saturation range; (2) the incorporation of phase behaviors under pore confinement into the LB numerical scheme; and (3) the use of additional larger REVs or whole cores for modeling through mesh dependence analysis, if computational resources permit.

Although one lattice in the computational domain is represented by one voxel of 3D digital rock images in this study, we have to admit that mesh dependence analysis is necessary in many cases to be conducted on rock images before LB simulations for fine characterization of complex pore structures, fluid–fluid, and fluid–solid interactions, if computational resources are abundant. Furthermore, mesh dependence analysis is typically essential for multiphase flow until an optimum resolution is asserted for defining the effective interface thickness in lattice unit and reducing the spurious velocity magnitude of the LB implementations so as to capture as enough flow details at pore scale as possible. For further and detailed instructions on how to embark on mesh dependence analysis for LB simulations, one is encouraged to refer to [83].

Author Contributions: Conceptualization and methodology, Y.W., W.Z.; LB algorithms and implementation, Y.W. and W.Z.; Data curation and visualization, Y.W., W.Z. and L.J.; formal analysis and investigation, Y.W., W.Z. and Z.C.; writing the manuscript, Y.W. and W.Z.; funding acquisition, and project administration, C.J. All authors have read and agreed to the published version of the manuscript.

Funding: This research received no external funding.

Institutional Review Board Statement: Not applicable.

Informed Consent Statement: Not applicable.

Data Availability Statement: Not applicable.

Acknowledgments: This work is supported by CNPC Scientific Research and Technology Development Project “Whole petroleum system theory and unconventional hydrocarbon accumulation mechanism” (2021DJ0101).

Conflicts of Interest: The authors declare no conflict of interest.

References

1. Huang, L.; Zhou, W.; Xu, H.; Wang, L.; Zou, J.; Zhou, Q. Dynamic fluid states in organic-inorganic nanocomposite: Implications for shale gas recovery and CO₂ sequestration. *Chem. Eng. J.* **2021**, *411*, 128423. [[CrossRef](#)]
2. Pörtner, H.-O.; Roberts, D.C.; Adams, H.; Adler, C.; Aldunce, P.; Ali, E.; Begum, R.A.; Betts, R.; Kerr, R.B.; Biesbroek, R. *Climate Change 2022: Impacts, Adaptation and Vulnerability*; IPCC Sixth Assessment Report 2022; IPCC: Geneva, Switzerland, 2022.
3. Matos, S.; Viardot, E.; Sovacool, B.K.; Geels, F.W.; Xiong, Y. Innovation and climate change: A review and introduction to the Special Issue. *Technovation* **2022**, *117*, 102612. [[CrossRef](#)]
4. Liu, B.; Qin, J.; Shi, J.; Jiang, J.; Wu, X.; He, Z. New perspectives on utilization of CO₂ sequestration technologies in cement-based materials. *Constr. Build. Mater.* **2021**, *272*, 121660. [[CrossRef](#)]
5. McClure, J.E.; Li, Z.; Berrill, M.; Ramstad, T. The LBPM software package for simulating multiphase flow on digital images of porous rocks. *Comput. Geosci.* **2021**, *25*, 871–895. [[CrossRef](#)]

6. Lichtschlag, A.; Pearce, C.R.; Suominen, M.; Blackford, J.; Borisov, S.M.; Bull, J.M.; de Beer, D.; Dean, M.; Esposito, M.; Flohr, A. Suitability analysis and revised strategies for marine environmental carbon capture and storage (CCS) monitoring. *Int. J. Greenh. Gas Control* **2021**, *112*, 103510. [[CrossRef](#)]
7. Paltsev, S.; Morris, J.; Kheshgi, H.; Herzog, H. Hard-to-Abate Sectors: The role of industrial carbon capture and storage (CCS) in emission mitigation. *Appl. Energy* **2021**, *300*, 117322. [[CrossRef](#)]
8. Mouahid, A.; Bombarda, I.; Claeys-Bruno, M.; Amat, S.; Myotte, E.; Nisteron, J.-P.; Crampon, C.; Badens, E. Supercritical CO₂ extraction of Moroccan argan (*Argania spinosa* L.) oil: Extraction kinetics and solubility determination. *J. CO₂ Util.* **2021**, *46*, 101458. [[CrossRef](#)]
9. Bakhshian, S.; Hosseini, S.A. Pore-scale analysis of supercritical CO₂-brine immiscible displacement under fractional-wettability conditions. *Adv. Water Resour.* **2019**, *126*, 96–107. [[CrossRef](#)]
10. Ershadnia, R.; Hajirezaie, S.; Amooie, A.; Wallace, C.D.; Gershenzon, N.I.; Hosseini, S.A.; Sturmer, D.M.; Ritzi, R.W.; Soltanian, M.R. CO₂ geological sequestration in multiscale heterogeneous aquifers: Effects of heterogeneity, connectivity, impurity, and hysteresis. *Adv. Water Resour.* **2021**, *151*, 103895. [[CrossRef](#)]
11. Hou, L.; Yu, Z.; Luo, X.; Wu, S. Self-sealing of caprocks during CO₂ geological sequestration. *Energy* **2022**, *252*, 124064. [[CrossRef](#)]
12. Ali, M.; Al-Yaseri, A.; Awan, F.U.R.; Arif, M.; Keshavarz, A.; Iglauer, S. Effect of water-soluble organic acids on wettability of sandstone formations using streaming zeta potential and NMR techniques: Implications for CO₂ geo-sequestration. *Fuel* **2022**, *329*, 125449. [[CrossRef](#)]
13. Teng, Y.; Wang, P.; Xie, H.; Zhu, J. Capillary trapping characteristics of CO₂ sequestration in fractured carbonate rock and sandstone using MRI. *J. Nat. Gas Sci. Eng.* **2022**, *108*, 104809. [[CrossRef](#)]
14. Abd Rahman, I.; Hasbollah, D.A.; Yunus, N.M.; Kasiman, E.; Mazlan, A. In Carbon Dioxide Storage Potential in Malaysian Sandstone Aquifer: An Overview. *IOP Conf. Series: Earth Environ. Sci.* **2022**, *971*, 012022. [[CrossRef](#)]
15. Gorecki, C.D.; Sorensen, J.A.; Bremer, J.M.; Knudsen, D.J.; Smith, S.A.; Steadman, E.N.; Harju, J.A. Development of storage coefficients for determining the effective CO₂ storage resource in deep saline formations. In Proceedings of the SPE International Conference on CO₂ Capture, Storage, and Utilization, San Diego, CA, USA, 2–4 November 2009; OnePetro: Richardson, TX, USA, 2009.
16. Page, S.; Williamson, A.; Mason, I. Carbon capture and storage: Fundamental thermodynamics and current technology. *Energy Policy* **2009**, *37*, 3314–3324. [[CrossRef](#)]
17. Jin, C.; Liu, L.; Li, Y.; Zeng, R. Capacity assessment of CO₂ storage in deep saline aquifers by mineral trapping and the implications for Songliao Basin, Northeast China. *Energy Sci. Eng.* **2017**, *5*, 81–89. [[CrossRef](#)]
18. Yanzhong, W.; Nianmin, Z.; Xu, C.; Yingchang, C.; Guanghui, Y.; Gluyas, J.G.; Miruo, L. Geologic CO₂ storage in arkosic sandstones with CaCl₂-rich formation water. *Chem. Geol.* **2020**, *558*, 119867. [[CrossRef](#)]
19. Koukouzas, N.; Kypritidou, Z.; Purser, G.; Rochelle, C.A.; Vasilatos, C.; Tsoukalas, N. Assessment of the impact of CO₂ storage in sandstone formations by experimental studies and geochemical modeling: The case of the Mesohellenic Trough, NW Greece. *Int. J. Greenh. Gas Control* **2018**, *71*, 116–132. [[CrossRef](#)]
20. Alemu, B.L.; Aagaard, P.; Munz, I.A.; Skurtveit, E. Caprock interaction with CO₂: A laboratory study of reactivity of shale with supercritical CO₂ and brine. *Appl. Geochem.* **2011**, *26*, 1975–1989. [[CrossRef](#)]
21. Huq, F.; Blum, P.; Marks, M.A.; Nowak, M.; Haderlein, S.B.; Grathwohl, P. Chemical changes in fluid composition due to CO₂ injection in the Altmark gas field: Preliminary results from batch experiments. *Environ. Earth Sci.* **2012**, *67*, 385–394. [[CrossRef](#)]
22. Garcia-Rios, M.; Luquot, L.; Soler, J.M.; Cama, J. Laboratory-scale interaction between CO₂-rich brine and reservoir rocks (limestone and sandstone). *Procedia Earth Planet. Sci.* **2013**, *7*, 109–112. [[CrossRef](#)]
23. Liu, Q.; Zhu, D.; Jin, Z.; Tian, H.; Zhou, B.; Jiang, P.; Meng, Q.; Wu, X.; Xu, H.; Hu, T. Carbon capture and storage for long-term and safe sealing with constrained natural CO₂ analogs. *Renew. Sustain. Energy Rev.* **2023**, *171*, 113000. [[CrossRef](#)]
24. Ning, Y.; Tura, A. Wellbore Integrity Impact on Carbon Leakage to Ensure Safe Geological Sequestration. In Proceedings of the SPE Annual Technical Conference and Exhibition, Houston, TX, USA, 3–5 October 2022; OnePetro: Richardson, TX, USA, 2022.
25. Ding, K.; Wang, L.; Ren, B.; Li, Z.; Wang, S.; Jiang, C. Experimental study on relative permeability characteristics for CO₂ in sandstone under high temperature and overburden pressure. *Minerals* **2021**, *11*, 956. [[CrossRef](#)]
26. Gholami, R.; Raza, A.; Iglauer, S. Leakage risk assessment of a CO₂ storage site: A review. *Earth-Sci. Rev.* **2021**, *223*, 103849. [[CrossRef](#)]
27. Moradi, B.; Hosseini Moghadam, A.; Rasaei, M.R.; Papi, A. Pore-scale characterization of CO₂ front progress through a porous medium using a free energy model based on Phase-Field Lattice Boltzmann Method. *J. Pet. Sci. Eng.* **2022**, *210*, 110008. [[CrossRef](#)]
28. Kohanpur, A.H.; Rahromostaqim, M.; Valocchi, A.J.; Sahimi, M. Two-phase flow of CO₂-brine in a heterogeneous sandstone: Characterization of the rock and comparison of the lattice-Boltzmann, pore-network, and direct numerical simulation methods. *Adv. Water Resour.* **2020**, *135*, 103469. [[CrossRef](#)]
29. Tahmasebi, P.; Sahimi, M.; Kohanpur, A.H.; Valocchi, A. Pore-scale simulation of flow of CO₂ and brine in reconstructed and actual 3D rock cores. *J. Pet. Sci. Eng.* **2017**, *155*, 21–33. [[CrossRef](#)]
30. Akbarabadi, M.; Piri, M. Relative permeability hysteresis and capillary trapping characteristics of supercritical CO₂/brine systems: An experimental study at reservoir conditions. *Adv. Water Resour.* **2013**, *52*, 190–206. [[CrossRef](#)]
31. Liu, F.; Lu, P.; Griffith, C.; Hedges, S.W.; Soong, Y.; Hellevang, H.; Zhu, C. CO₂-brine-caprock interaction: Reactivity experiments on Eau Claire shale and a review of relevant literature. *Int. J. Greenh. Gas Control* **2012**, *7*, 153–167. [[CrossRef](#)]

32. Tsakiroglou, C.; Avraam, D.; Payatakes, A. Transient and steady-state relative permeabilities from two-phase flow experiments in planar pore networks. *Adv. Water Resour.* **2007**, *30*, 1981–1992. [[CrossRef](#)]
33. Suwandi, N.; Jiang, F.; Tsuji, T. Relative Permeability Variation Depending on Viscosity Ratio and Capillary Number. *Water Resour. Res.* **2022**, *58*, e2021WR031501. [[CrossRef](#)]
34. Fan, M.; Dalton, L.E.; McClure, J.; Ripepi, N.; Westman, E.; Crandall, D.; Chen, C. Comprehensive study of the interactions between the critical dimensionless numbers associated with multiphase flow in 3D porous media. *Fuel* **2019**, *252*, 522–533. [[CrossRef](#)]
35. Liu, Z.; Wu, H. Pore-scale modeling of immiscible two-phase flow in complex porous media. *Appl. Therm. Eng.* **2016**, *93*, 1394–1402. [[CrossRef](#)]
36. Müller, N. Supercritical CO₂-brine relative permeability experiments in reservoir rocks—Literature review and recommendations. *Transp. Porous Media* **2011**, *87*, 367–383. [[CrossRef](#)]
37. Carrillo, F.J.; Bourg, I.C.; Soulaine, C. Multiphase flow modeling in multiscale porous media: An open-source micro-continuum approach. *J. Comput. Phys. X* **2020**, *8*, 100073. [[CrossRef](#)]
38. Wang, J. Continuum theory for dense gas-solid flow: A state-of-the-art review. *Chem. Eng. Sci.* **2020**, *215*, 115428. [[CrossRef](#)]
39. Papp, J.; Wilmoth, R.; Chartrand, C.; Dash, S. Simulation of high-altitude plume flow fields using a hybrid continuum CFD/DSMC approach. In Proceedings of the 42nd AIAA/ASME/SAE/ASEE Joint Propulsion Conference & Exhibit, Sacramento, CA, USA, 9–12 July 2006; p. 4412.
40. Wang, S.; Ruspini, L.C.; Øren, P.E.; Van Offenwert, S.; Bultreys, T. Anchoring Multi-Scale Models to Micron-Scale Imaging of Multiphase Flow in Rocks. *Water Resour. Res.* **2022**, *58*, e2021WR030870. [[CrossRef](#)]
41. Masalmeh, S.K.; Jing, X.; Roth, S.; Wang, C.; Dong, H.; Blunt, M. Towards predicting multi-phase flow in porous media using digital rock physics: Workflow to test the predictive capability of pore-scale modeling. In Proceedings of the Abu Dhabi International Petroleum Exhibition and Conference, Abu Dhabi, United Arab Emirates, 9–12 November 2015; OnePetro: Richardson, TX, USA, 2015.
42. Dinariev, O.; Evseev, N. Multiphase flow modeling with density functional method. *Comput. Geosci.* **2016**, *20*, 835–856. [[CrossRef](#)]
43. Koroteev, D.; Dinariev, O.; Evseev, N.; Klemin, D.; Nadeev, A.; Safonov, S.; Gurpinar, O.; Berg, S.; Van Kruijsdijk, C.; Armstrong, R. Direct hydrodynamic simulation of multiphase flow in porous rock. *Petrophysics-SPWLA J. Form. Eval. Reserv. Descr.* **2014**, *55*, 294–303.
44. Blunt, M.J.; Bijeljic, B.; Dong, H.; Gharbi, O.; Iglauer, S.; Mostaghimi, P.; Paluszny, A.; Pentland, C. Pore-scale imaging and modelling. *Adv. Water Resour.* **2013**, *51*, 197–216. [[CrossRef](#)]
45. Øren, P.-E.; Bakke, S. Reconstruction of Berea sandstone and pore-scale modelling of wettability effects. *J. Pet. Sci. Eng.* **2003**, *39*, 177–199. [[CrossRef](#)]
46. Valvatne, P.H.; Blunt, M.J. Predictive pore-scale modeling of two-phase flow in mixed wet media. *Water Resour. Res.* **2004**, *40*, W07406. [[CrossRef](#)]
47. Blunt, M.J.; Jackson, M.D.; Piri, M.; Valvatne, P.H. Detailed physics, predictive capabilities and macroscopic consequences for pore-network models of multiphase flow. *Adv. Water Resour.* **2002**, *25*, 1069–1089. [[CrossRef](#)]
48. Ramstad, T.; Øren, P.-E.; Bakke, S. Simulation of two-phase flow in reservoir rocks using a lattice Boltzmann method. *SPE J.* **2010**, *15*, 917–927. [[CrossRef](#)]
49. Kelly, S.; El-Sobky, H.; Torres-Verdín, C.; Balhoff, M.T. Assessing the utility of FIB-SEM images for shale digital rock physics. *Adv. Water Resour.* **2016**, *95*, 302–316. [[CrossRef](#)]
50. Liang, Z.; Fernandes, C.; Magnani, F.; Philippi, P. A reconstruction technique for three-dimensional porous media using image analysis and Fourier transforms. *J. Pet. Sci. Eng.* **1998**, *21*, 273–283. [[CrossRef](#)]
51. Zhou, X.-P.; Xiao, N. 3D numerical reconstruction of porous sandstone using improved simulated annealing algorithms. *Rock Mech. Rock Eng.* **2018**, *51*, 2135–2151. [[CrossRef](#)]
52. Lin, W.; Li, X.; Yang, Z.; Xiong, S.; Luo, Y.; Zhao, X. Modeling of 3D rock porous media by combining X-ray CT and Markov chain Monte Carlo. *J. Energy Resour. Technol.* **2020**, *142*, 013001. [[CrossRef](#)]
53. Xie, Y.; Luo, Z.; Cheng, L.; Zhao, L.; Chen, X.; Zhang, N.; Ren, D.; Cao, Y. Numerical modeling and analysis of the matrix acidizing process in fractured sandstone rocks with the Extended-FEM. *J. Pet. Sci. Eng.* **2023**, *220*, 111215. [[CrossRef](#)]
54. Huang, Y.; Zhou, Z.-f. Simulation of solute transport using a coupling model based on finite volume method in fractured rocks. *J. Hydrodyn.* **2010**, *22*, 129–136. [[CrossRef](#)]
55. Alpak, F.; Samardžić, A.; Frank, F. A distributed parallel direct simulator for pore-scale two-phase flow on digital rock images using a finite difference implementation of the phase-field method. *J. Pet. Sci. Eng.* **2018**, *166*, 806–824. [[CrossRef](#)]
56. Gresho, P.M. Some current CFD issues relevant to the incompressible Navier–Stokes equations. *Comput. Methods Appl. Mech. Eng.* **1991**, *87*, 201–252. [[CrossRef](#)]
57. Karniadakis, G.E.; Israeli, M.; Orszag, S.A. High-order splitting methods for the incompressible Navier–Stokes equations. *J. Comput. Phys.* **1991**, *97*, 414–443. [[CrossRef](#)]
58. Soleimani, R.; Norouzi, S.; Rasaei, M.R. Investigation of gas condensate drop-out effect on gas relative permeability by Lattice Boltzmann modelling. *Can. J. Chem. Eng.* **2019**, *97*, 1921–1930. [[CrossRef](#)]
59. Xu, A.; Shi, L.; Zhao, T. Accelerated lattice Boltzmann simulation using GPU and OpenACC with data management. *Int. J. Heat Mass Transf.* **2017**, *109*, 577–588. [[CrossRef](#)]

60. Huang, H.; Huang, J.-J.; Lu, X.-Y. Study of immiscible displacements in porous media using a color-gradient-based multiphase lattice Boltzmann method. *Comput. Fluids* **2014**, *93*, 164–172. [[CrossRef](#)]
61. Chen, L.; Kang, Q.; Mu, Y.; He, Y.-L.; Tao, W.-Q. A critical review of the pseudopotential multiphase lattice Boltzmann model: Methods and applications. *Int. J. Heat Mass Transf.* **2014**, *76*, 210–236. [[CrossRef](#)]
62. Pooley, C.; Furtado, K. Eliminating spurious velocities in the free-energy lattice Boltzmann method. *Phys. Rev. E* **2008**, *77*, 046702. [[CrossRef](#)]
63. Huang, H.; Wang, L.; Lu, X.-y. Evaluation of three lattice Boltzmann models for multiphase flows in porous media. *Comput. Math. Appl.* **2011**, *61*, 3606–3617. [[CrossRef](#)]
64. Tian, Z.; Xing, H.; Tan, Y.; Gao, J. A coupled lattice Boltzmann model for simulating reactive transport in CO₂ injection. *Phys. A: Stat. Mech. Its Appl.* **2014**, *403*, 155–164. [[CrossRef](#)]
65. Cameron, K.C.; Buchan, G.D. Darcys Law. In *SW Encyclopedia of Water Science*; Trimble: Westminster, CO, USA, 2008; pp. 143–146.
66. Gasmı, H.; Khan, U.; Zaib, A.; Ishak, A.; Eldin, S.M.; Raizah, Z. Analysis of Mixed Convection on Two-Phase Nanofluid Flow Past a Vertical Plate in Brinkman-Extended Darcy Porous Medium with Nield Conditions. *Mathematics* **2022**, *10*, 3918. [[CrossRef](#)]
67. Zhang, Q.; Choo, J.; Borja, R.I. On the preferential flow patterns induced by transverse isotropy and non-Darcy flow in double porosity media. *Comput. Methods Appl. Mech.* **2019**, *353*, 570–592. [[CrossRef](#)]
68. Zhu, W.; Liu, Y.; Shi, Y.; Zou, G.; Zhang, Q.; Kong, D. Effect of dynamic threshold pressure gradient on production performance in water-bearing tight gas reservoir. *Adv. Geo-Energy Res.* **2022**, *6*, 286. [[CrossRef](#)]
69. Lu, C.; Qin, X.; Ma, C.; Yu, L.; Geng, L.; Bian, H.; Zhang, K.; Zhou, Y. Investigation of the impact of threshold pressure gradient on gas production from hydrate deposits. *Fuel* **2022**, *319*, 123569. [[CrossRef](#)]
70. Li, D.; Zha, W.; Liu, S.; Wang, L.; Lu, D. Pressure transient analysis of low permeability reservoir with pseudo threshold pressure gradient. *J. Pet. Sci. Eng.* **2016**, *147*, 308–316. [[CrossRef](#)]
71. Hao, F.; Cheng, L.; Hassan, O.; Hou, J.; Liu, C.; Feng, J. Threshold pressure gradient in ultra-low permeability reservoirs. *Pet. Sci. Technol.* **2008**, *26*, 1024–1035. [[CrossRef](#)]
72. Christopoulou, M.A.; Koutsovitis, P.; Kostoglou, N.; Paraskevopoulou, C.; Sideridis, A.; Petrounias, P.; Rogkala, A.; Stock, S.; Koukoulas, N. Evaluation of the CO₂ Storage Capacity in Sandstone Formations from the Southeast Mesohellenic trough (Greece). *Energies* **2022**, *15*, 3491. [[CrossRef](#)]
73. Ni, P.; Wang, S.; Wang, C.; Zhang, S. Estimation of REV size for fractured rock mass based on damage coefficient. *Rock Mech. Rock Eng.* **2017**, *50*, 555–570. [[CrossRef](#)]
74. Min, K.-B.; Jing, L.; Stephansson, O. Determining the equivalent permeability tensor for fractured rock masses using a stochastic REV approach: Method and application to the field data from Sellafeld, UK. *Hydrogeol. J.* **2004**, *12*, 497–510. [[CrossRef](#)]
75. Boek, E.S.; Venturoli, M. Lattice-Boltzmann studies of fluid flow in porous media with realistic rock geometries. *Comput. Math. Appl.* **2010**, *59*, 2305–2314. [[CrossRef](#)]
76. Xing, H.; Gao, J.; Zhang, J.; Liu, Y. Towards an integrated simulator for enhanced geothermal reservoirs. In Proceedings of the World Geothermal Congress 2010, Bali, Indonesia, 25–29 April 2010.
77. Ziegler, D.P. Boundary conditions for lattice Boltzmann simulations. *J. Stat. Phys.* **1993**, *71*, 1171–1177. [[CrossRef](#)]
78. Ju, Y.; Wang, J.; Gao, F.; Xie, H. Lattice-Boltzmann simulation of microscale CH₄ flow in porous rock subject to force-induced deformation. *Chin. Sci. Bull.* **2014**, *59*, 3292–3303. [[CrossRef](#)]
79. Zhao, W.; Jia, C.; Zhang, T.; Jiang, L.; Li, X.; Jiang, Z.; Zhang, F. Effects of nanopore geometry on confined water flow: A view of lattice Boltzmann simulation. *Chem. Eng. Sci.* **2021**, *230*, 116183. [[CrossRef](#)]
80. Bhatnagar, P.L.; Gross, E.P.; Krook, M. A model for collision processes in gases. I. Small amplitude processes in charged and neutral one-component systems. *Phys. Rev.* **1954**, *94*, 511. [[CrossRef](#)]
81. Gunstensen, A.K.; Rothman, D.H.; Zaleski, S.; Zanetti, G. Lattice Boltzmann model of immiscible fluids. *Phys. Rev. A* **1991**, *43*, 4320–4327. [[CrossRef](#)]
82. Iglauer, S.; Pentland, C.; Busch, A. CO₂ wettability of seal and reservoir rocks and the implications for carbon geo-sequestration. *Water Resour. Res.* **2015**, *51*, 729–774. [[CrossRef](#)]
83. Vasheghani Farahani, M.; Hassanpouryouzband, A.; Yang, J.; Tohidi, B. Heat transfer in unfrozen and frozen porous media: Experimental measurement and pore-scale modeling. *Water Resour. Res.* **2020**, *56*, e2020WR027885. [[CrossRef](#)]

Disclaimer/Publisher’s Note: The statements, opinions and data contained in all publications are solely those of the individual author(s) and contributor(s) and not of MDPI and/or the editor(s). MDPI and/or the editor(s) disclaim responsibility for any injury to people or property resulting from any ideas, methods, instructions or products referred to in the content.